PHYSICAL REVIEW D **105,** 083009 (2022)

Editors' Suggestion **Featured in Physics**

Mapping the Universe in hydrogen deuteride

Patrick C. Breysse,[1,*] Simon Foreman,[2,3] Laura C. Keating,[4] Joel Meyers,[5] and Norman Murray[6]

[1] *Center for Cosmology and Particle Physics, Department of Physics, New York University,
726 Broadway, New York, New York 10003, USA*

[2] *Perimeter Institute for Theoretical Physics, 31 Caroline Street North, Waterloo,
Ontario N2L 2Y5, Canada*

[3] *Dominion Radio Astrophysical Observatory, Herzberg Astronomy and Astrophysics Research Centre,
National Research Council Canada, P.O. Box 248, Penticton, British Columbia V2A 6J9, Canada*

[4] *Leibniz-Institut für Astrophysik Potsdam (AIP), An der Sternwarte 16, D-14482 Potsdam, Germany*

[5] *Department of Physics, Southern Methodist University, 3215 Daniel Ave, Dallas, Texas 75275, USA*

[6] *Canadian Institute for Theoretical Astrophysics, University of Toronto,
60 St. George Street, Toronto M5S 3H8, Canada*

(Received 13 May 2021; accepted 9 March 2022; published 15 April 2022)

Hydrogen deuteride (HD) is prevalent in a wide variety of astrophysical environments, and measuring its large-scale distribution at different epochs can, in principle, provide information about the properties of these environments. In this paper we explore the prospects for accessing this distribution using line-intensity mapping of emission from the lowest rotational transition in HD, focusing on observations of the epoch of reionization ($z \sim 6$–10) and earlier. We find the signal from the epoch of reionization to be most promising, through cross correlations within existing [CII] intensity mapping surveys. While the signal we predict is out of reach for current-generation projects, planned future improvements should be able to detect reionization-era HD without any additional observations, and would help to constrain the properties of the star-forming galaxies thought to play a key role in reionization. We also investigate several avenues for measuring HD during "cosmic dawn" ($z \sim 10$–30), a period in which HD could provide one of the only complementary observables to 21 cm intensity maps. We conclude that existing and planned facilities are poorly matched to the specifications desirable for a significant detection, though such a measurement may be achievable with sustained future effort. Finally, we explain why HD intensity mapping of the intergalactic medium during the cosmic dark ages ($z \gtrsim 30$) appears to be out of reach of any conceivable experiment.

DOI: 10.1103/PhysRevD.105.083009

I. INTRODUCTION

Line-intensity mapping, the measurement of the integrated flux of spectral lines emitted from galaxies or the intergalactic medium, is a rapidly growing field with wide-ranging applications in cosmology and astrophysics [1,2]. By observing spatial fluctuations in the emission, intensity-mapping surveys are able to make use of the emission of many unresolved galaxies, rather than identifying individual objects above some flux cut. Accurate redshifts can typically be obtained due to the sharp spectral features which are observed, thereby allowing surveys to produce three-dimensional maps of structure of the Universe as traced by the total flux of some emission line.

Several spectral lines have been identified as potential targets of line-intensity mapping surveys [3]. The 21 cm line resulting from the spin-flip transition of neutral hydrogen has been the focus of a great deal of study (see Refs. [4,5] for reviews), while the CO rotational lines, the [CII] fine-structure line, and the Lyα line have begun to receive increased attention [1,2].

Molecular hydrogen (H_2) is by far the most abundant molecule in the Universe. Molecular gas is the main driver of star formation, and knowledge of its density is key to understanding the interstellar medium, star formation history, and galaxy evolution [6]. Unfortunately, H_2 possesses no permanent electric dipole moment and therefore has only quadrupolar rotational transitions ($\Delta J = 2$). The lowest of these rotational states lies about 510 K above ground, and the spontaneous decay time is on the order of 100 yr, making it a faint line visible only in hot environments. These factors make H_2 a challenging target for line-intensity mapping, and we will quantify just how challenging as part of this work.

Carbon and oxygen are among the most abundant elements in galaxies, and combine to form CO in molecular clouds. CO possesses a modest dipole moment (0.11 D) and

---

[*] pb2555@nyu.edu

low excitation energy for the ground rotational transition ($h\nu/k_B = 5.53$ K), which means that even in the cold environments of molecular clouds, CO rotational states are easily excited. The emission from rotational transitions of CO also falls in convenient atmospheric windows (115.27 GHz or 2.6 mm for the 1-0 transition), making CO an excellent candidate for line-intensity mapping surveys. The prevalence and observability of CO have made it a common observational target, and have motivated many attempts to use the CO density as a tracer of the molecular gas density through the CO-to-H_2 conversion factor [7]. This conversion factor has a relatively large systematic uncertainty in our own galaxy, depends on the environment, and is less certain in other galaxies and at higher redshifts. CO intensity mapping surveys have the potential to probe the properties of high-redshift galaxies on the faint end of the luminosity function and to study the gas density and star formation rate of these poorly understood objects [8,9].

Here we discuss another potential line-intensity mapping target which is abundant, prevalent, and directly traces the density of molecular hydrogen. Hydrogen deuteride (HD) has a weak permanent electric dipole moment [10] due to the proton-deuteron mass difference, which causes the electrons to orbit more closely around the latter, giving the ground state 8.56×10^{-4} D [11]. The 1-0 rotational transition of HD lies at 2.675 THz (112 μm), which is strongly absorbed in the atmosphere, making it very difficult to observe from the ground. The excitation energy for the ground rotational state is fairly high ($h\nu/k_B = 128$ K) compared to that of CO. Rotational transitions of HD in emission have been observed with ISO [12–14], UKIRT [15], the Spitzer Space Telescope [16,17], and the Herschel Space Observatory [18], and have also been seen in absorption spectra of quasars [19] and within the Milky Way (e.g., Refs. [20–24]). The HD(1-0) line is also a key target of the Origins Space Telescope for measuring the masses of protoplanetary disks [25].

Deuterium was produced in the first few minutes of the radiation-dominated era in the process of big bang nucleosynthesis (BBN) [26]. There are no known astrophysical sources of deuterium, and so essentially all deuterium in the Universe is of primordial origin [27,28]. Deuterium is burned in stars, and so the deuterium abundance has decreased monotonically from its primordial value throughout the history of the Universe. The primordial deuterium abundance has been measured to be $(\mathrm{D/H})_p = (2.527 \pm 0.030) \times 10^{-5}$ [29] in good agreement with the value predicted theoretically by standard BBN [30] when using the photon-to-baryon ratio as determined from measurements of the cosmic microwave background (CMB) made by the Planck satellite [31].

Hydrogen deuteride formed well before reionization, and significant fractionation resulted in a freeze-out ratio of $\mathrm{HD/H_2} \approx 7 \times 10^{-4}$ by $z \approx 40$, a factor of about 25 larger than the primordial D/H ratio [32]. HD is therefore expected to be present with a significant abundance in essentially all galaxies at all redshifts, even in the pristine primordial environments of the first collapsed objects (depending on environmental factors, such as the ionizing background radiation at the relevant epoch).

Several upcoming surveys aim to perform intensity mapping of the [CII] fine structure line at 1.901 THz (158 μm) over a wide range of redshifts (see Ref. [1] for a summary). These same experiments are capable of doing intensity mapping with the HD(1-0) rotational line in a higher redshift window. For example, the Fred Young Submillimeter Telescope (FYST, [33][1]) is capable of observing the redshifted [CII] line in the window $5 < z < 9$, which would allow for intensity mapping of HD in the range $7.5 < z < 13$. It is particularly useful that there is a range of redshifts $7.5 < z < 9$ where both [CII] and HD will be visible with FYST, which allows for cross correlations using maps obtained by the same instrument.

In this work, we investigate the prospects for detection of an HD(1-0) line intensity signal from three different eras: reionization ($z \sim 6$–10), cosmic dawn ($z \sim 10$–30), and the dark ages ($z \gtrsim 30$). A measurement from each era would provide distinct information: the signal from reionization would tell us about the star-forming galaxies thought to play a key role in the creation of ionizing bubbles of radiation; the signal from cosmic dawn would tell us about the conditions in the minihalos that host the first generation of stars; and the signal from the dark ages would provide us with information about density fluctuations in the intergalactic medium, which would directly trace cosmological perturbations in the same way envisioned for dark-ages 21 cm measurements [34].

We find the signal from reionization to be the most promising for detection: while likely out of reach of the planned [CII] survey by FYST, a much more ambitious "Stage II" [CII] survey would be capable of SNR ~ 11 for even our most pessimistic model. While this number corresponds to raw statistical significance only, ignoring the details of foreground subtraction and other systematics, we nevertheless see it as an encouraging sign that HD(1-0) may be observable by intensity mapping surveys intended for [CII].

For cosmic dawn, we examine several observational strategies, and conclude that existing and planned facilities are poorly matched to the specifications desirable for making an intensity map of HD(1-0): only several years' worth of ALMA observing time over a 0.01 deg^2 patch or CMB-HiDef [35] observing time over a few deg^2 patch would have any chance of detecting the HD(1-0) autopower spectrum. Possibilities for cross correlations are limited, and will not fare any better with current or planned experiments. Even when considering a space mission like the proposed PIXIE satellite [36], it would take an extremely futuristic sensitivity improvement for an HD autospectrum measurement, similar

---

[1] www.ccatobservatory.org.

to what is needed to detect time evolution of the CMB blackbody temperature [37].

Finally, HD(1-0) intensity mapping in the dark ages appears to be completely infeasible, due primarily to the high energy (compared to 21 cm in HI) required to excite HD into the first rotational state, along with the low abundance of HD (again compared to HI).

This paper is organized as follows. In Sec. II we present a model for the HD(1-0) line intensity autospectrum, and cross spectrum with [CII], based on radiative transfer and estimates of the total abundance of molecular gas, and forecast their detectability by FYST and a next-generation [CII] intensity mapping survey. In Sec. III we adapt the halo model for H_2 intensity mapping from Ref. [38] to HD at cosmic dawn, and discuss a variety of possible observing strategies. In Sec. IV we estimate the strength of HD(1-0) emission from the intergalactic medium during the dark ages, and then we conclude in Sec. V. Appendixes A and C contain extra details about our forecasts, while Appendix B consists of H_2 cosmic-dawn intensity mapping forecasts, based on Ref. [38] but with updated model ingredients and instrumental specifications.

For all computations, we use cosmological parameters from the Planck 2015 results, given in the "TT, TE, EE + lowP + lensing + ext" column of Table 4 of Ref. [31].

II. REIONIZATION

A. Radiative transfer

Here we present an estimate of the HD intensity mapping signal during reionization, based on simple radiative transfer arguments.

Consider a line of sight through an HD-emitting galaxy with total optical depth τ in a given rotational transition. A cosmologically-nearby observer will see an intensity

$$I_{\mathrm{HD}} = \int_0^\tau \frac{j_{\mathrm{HD}}(\tau')}{\kappa_{\mathrm{HD}}(\tau')} e^{-\tau'} d\tau', \tag{1}$$

where j_{HD} and κ_{HD} are the emission and absorption coefficients and we have neglected background radiation and assumed that our observation has a frequency resolution wider than the target line. For a line of width $\Delta\nu$ in local thermodynamic equilibrium (LTE), $j_{\mathrm{HD}}/\kappa_{\mathrm{HD}} = B_\nu(T)\Delta\nu$, where B_ν is the Planck function at excitation temperature T. We then have

$$I_{\mathrm{HD}} = B_\nu(T)\Delta\nu(1-e^{\tau}) = B_\nu(T)\Delta\nu(1-e^{N_\ell \sigma_{\mathrm{HD}}}), \tag{2}$$

where N_ℓ is the column density of HD molecules in the lower state of our transition and σ_{HD} is the cross section for the transition, given by [39]

$$\sigma_{\mathrm{HD}} = \frac{3c^2 A_{u\ell}}{8\pi\nu_{\mathrm{HD}}^2 \Delta\nu}(1-e^{-h\nu_{\mathrm{HD}}/k_{\mathrm{B}}T}). \tag{3}$$

The Einstein coefficient $A_{u\ell}$ for the HD(1-0) transition is 5.1×10^{-8} s^{-1} [40]. The line width $\Delta\nu$ will cancel out of our final expression, so we do not need to assign it a value.

Under the continued assumption of LTE, the total column density N_{HD} of HD molecules can be inferred from

$$\frac{N_\ell}{N_{\mathrm{HD}}} = \frac{2J+1}{Z_{\mathrm{HD}}} e^{hB_{\mathrm{HD}}J(J+1)/k_{\mathrm{B}}T}, \tag{4}$$

for a transition with lower rotational quantum number J. The rotational constant B_{HD} is 1.33×10^{12} s^{-1} [41]. The partition function Z_{HD} takes its usual form

$$Z_{\mathrm{HD}} = \sum_{J=0}^{\infty}(2J+1)e^{-hB_{\mathrm{HD}}J(J+1)/k_{\mathrm{B}}T}. \tag{5}$$

Combining Eqs. (2)–(5) yields

$$\begin{aligned} I_{\mathrm{HD}} &= \frac{2h\nu_{\mathrm{HD}}^4 \Delta v}{c^3}\frac{1-\exp(N_{\mathrm{HD}}\sigma_{\mathrm{HD}}/Z_{\mathrm{HD}})}{\exp(h\nu_{\mathrm{HD}}/k_{\mathrm{B}}T)-1} \\ &\approx C_{NI}(T)N_{\mathrm{HD}}, \end{aligned} \tag{6}$$

where we have defined

$$C_{NI}(T) \equiv \frac{2h\nu_{\mathrm{HD}}^4 \sigma_{\mathrm{HD}}(T)\Delta v}{c^3 Z_{\mathrm{HD}}(T)[\exp(h\nu_{\mathrm{HD}}/k_{\mathrm{B}}T)-1]}, \tag{7}$$

and assumed that the HD transition is optically thin in all regimes of interest.

We can verify this latter assumption by considering a typical molecular column through the Milky Way. If we define the HD/H_2 ratio $x_{\mathrm{HD/H2}} \equiv N_{\mathrm{HD}}/N_{\mathrm{H2}}$, we can express the HD optical depth in terms of the surface density Σ_{H2} of molecular hydrogen. In the extreme case wherein all of the HD is in the lower rotational state (i.e., $N_\ell = N_{\mathrm{HD}}$), the optical depth will be

$$\tau_{\mathrm{HD}}(N_\ell = N_{\mathrm{HD}}) = x_{\mathrm{HD/H2}}\sigma_{\mathrm{HD}}\frac{\Sigma_{\mathrm{H2}}}{m_{\mathrm{H2}}}, \tag{8}$$

where m_{H2} is the mass of a single H_2 molecule. We adopt $x_{\mathrm{HD/H2}} = 10^{-4}$ for the purposes of this section, which is broadly consistent with the models from Ref. [42]. For a typical Milky Way line of sight with $\Sigma_{\mathrm{H2}} \sim 10\ M_\odot$ pc^{-2} [43], we obtain

$$\tau_{\mathrm{HD}}(N_\ell = N_{\mathrm{HD}}) \sim 5\times10^{-4}\left(\frac{\Sigma_{\mathrm{H2}}}{10\ M_\odot/\mathrm{pc}^2}\right). \tag{9}$$

Because the transition is optically thin, the HD luminosity L_{HD} of a galaxy will simply scale as its total HD mass. Thus, again assuming a constant $x_{\mathrm{HD/H2}}$, we can write

$$L_{\mathrm{HD}} = 4\pi C_{NI}(T)x_{\mathrm{HD/H2}}\frac{M_{\mathrm{H2}}}{m_{\mathrm{H2}}}, \tag{10}$$

for a galaxy with total H_2 mass M_{H2}.

If we want to know the amplitude of the intensity mapping power spectrum, we need to integrate over the full distribution of halo luminosities,

$$\bar{I}_{\mathrm{HD}}(z)=\int_{M_{\mathrm{min}}}^{M_{\mathrm{max}}} dM\frac{dn}{dM}(z)\frac{L_{\mathrm{HD}}(M,z)}{4\pi D_{\mathrm{L}}(z)^2}y_{\mathrm{HD}}(z)D_{\mathrm{A}}(z)^2, \quad (11)$$

which, using Eq. (10), corresponds to integrating over the molecular gas content of the halos. In Eq. (11), M_{min} and M_{max} are the minimum and maximum masses of halos emitting in the given line, dn/dM is the halo mass function, D_{L} is the luminosity distance, D_{A} is the comoving angular diameter distance (equal to the comoving radial distance χ), and

$$y_{\mathrm{HD}}(z)\equiv\frac{d\chi}{d\nu_{\mathrm{HD}}}=\frac{\lambda_{\mathrm{HD}}(1+z)^2}{H(z)} \quad (12)$$

translates between χ and frequency, where λ_{HD} is the rest wavelength of HD(1-0). It is difficult to model the full distribution $M_{\mathrm{H2}}(M)$, due to uncertainties about conditions in high-redshift galaxies. However, in the absence of this information, we can reduce Eqs. (10)–(11) to

$$\bar{I}_{\mathrm{HD}}(z)=\frac{C_{NI}(T)x_{\mathrm{HD/H2}}y_{\mathrm{HD}}(z)D_{\mathrm{A}}(z)^2\rho_c(z)}{m_{\mathrm{H2}}D_{\mathrm{L}}(z)^2}\Omega_{\mathrm{H2}}(z), \quad (13)$$

where ρ_c is the critical cosmological density and Ω_{H2} is the total fraction of that density contributed by molecular gas. Thus we can estimate the strength of the HD signal from the total molecular gas content of the Universe.

Several of the quantities that go into Eq. (13) are highly uncertain even in the local Universe, and will be even more so at high redshift. It is therefore beyond our capabilities to claim a single estimate for the HD intensity. We will instead adopt a range of parameter values in an attempt to roughly quantify the range of possible signals. We will focus on two parameters which have a large impact on $\bar{I}_{\mathrm{HD}}$: the cosmological molecular gas abundance Ω_{H2} and the excitation temperature T.

For the molecular gas abundance, we rely on the simulated results presented in Ref. [44]. Figure 17 in Ref. [44] presents a range of possible Ω_{H2} values as a function of redshift. For our optimistic and pessimistic models we will use the highest and lowest values from these simulations, which correspond to the "Bau05.BR" and "Bow06.KMT" values[2] (at $z\sim6$, these are $\Omega_{\mathrm{H2}}\approx7\times10^{-4}$ and 1×10^{-4}). For the excitation temperature, we choose $T=20$ K for the pessimistic value and $T=50$ K for the optimistic model. The lower value is broadly consistent with conditions in local molecular clouds, while the higher is in rough agreement with the dust temperature obtained from the Planck Collaboration's modeling of the cosmic infrared background at $z\sim6$ [45]. Figure 1 shows the dependence of $\bar{I}_{\mathrm{HD}}$ on these two parameters, illustrating the range of models we consider. This clearly demonstrates the large amount of uncertainty on the strength of the HD signal, with ~2 orders of magnitude between the brightest and faintest intensities.

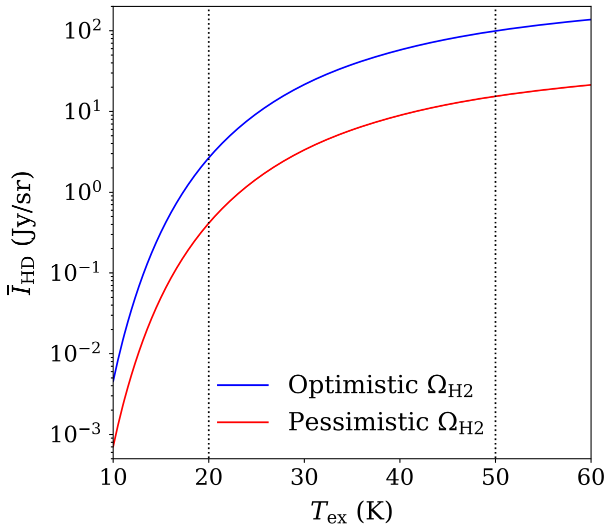

FIG. 1. Sky-averaged mean intensity of the HD line at $z=6$ computed using Eq. (13). Results are shown as a function of excitation temperature, with the optimistic and pessimistic values we assume marked with dotted lines. The blue and red curves assume the optimistic and pessimistic Ω_{H2} values, respectively, from Ref. [44].

B. The reionization-era power spectrum

Intensity maps are typically analyzed in terms of their power spectra. The power spectrum of line intensity fluctuations is the sum of contributions from large-scale clustering and Poisson shot noise,

$$P_X^{\mathrm{clus}}(k,z)=\bar{I}_X(z)^2\bar{b}_X(z)^2P_{\mathrm{m}}(k,z), \quad (14)$$

$$P_X^{\mathrm{shot}}(z)=\int_{M_{\mathrm{min}}}^{M_{\mathrm{max}}} dM\frac{dn}{dM}(z)\times\left[\frac{L_X(M,z)}{4\pi D_{\mathrm{L}}(z)^2}y_X(z)D_{\mathrm{A}}(z)^2\right]^2, \quad (15)$$

where we have used X to denote both the particle type and emission line we are considering [e.g., HD(1-0)]. The shape of the clustering term is set by the matter power spectrum P_{m}, and is weighted by the mean line intensity and the luminosity-weighted bias

---

[2] The main differences between these models relate to how star formation is suppressed in massive galaxies, the assumed stellar mass function for starbursts, and the implementation of star formation; see Ref. [44] for details.

$$\bar{b}_X(z) = \frac{\int_{M_{\min}}^{M_{\max}} dM \frac{dn}{dM}(z) L_X(M,z) b(M,z)}{\int_{M_{\min}}^{M_{\max}} dM \frac{dn}{dM}(z) L_X(M,z)}. \quad (16)$$

At the redshifts we consider here ($z \gtrsim 5$ or so), we expect structure growth to be relatively linear on scales that are clustering-dominated rather than shot-noise dominated. We thus expect the one-halo contribution to the power spectrum to be subdominant to the linear and shot-noise components. Further, any one-halo term will certainly be small compared to the uncertainty in our modeling. Thus, we neglect this term in our forecasts. We take $M_{\min} = 10^8\ M_\odot$ in this section, though as shown in Appendix A our power spectra are relatively insensitive to this choice. We choose an arbitrarily large value of $M_{\max} = 10^{15}\ M_\odot$ that is larger than the most massive halos we expect to see at these redshifts.

In order to fully model the power spectrum of HD fluctuations, we would need to understand how the global abundance of molecular gas is distributed in halos of different mass. The shot noise power in an HD survey would be

$$P_{\mathrm{HD}}^{\mathrm{shot}}(z) = C_{NI}^2(T)\left(\frac{x_{\mathrm{HD/H2}}}{m_{\mathrm{H2}}}\right)^2 \times \int dM \frac{dn}{dM}(z)\left[\frac{M_{\mathrm{H2}}(M)}{D_L^2(z)} y_{\mathrm{HD}}(z) D_A^2(z)\right]^2, \quad (17)$$

and the luminosity-weighted bias for HD would be given by

$$\bar{b}_{\mathrm{HD}} = \frac{\int dM M_{\mathrm{H2}}(M) b(M) dn/dM}{\int dM M_{\mathrm{H2}}(M) dn/dM}. \quad (18)$$

Estimating the full behavior of these quantities would require a functional form for $M_{\mathrm{H2}}(M)$, which we do not obtain from our radiative transfer model. However, given the uncertainty demonstrated above, the exact impact of changing $M_{\mathrm{H2}}(M)$ will likely be small compared to the difference in $\bar{I}_{\mathrm{HD}}$ values over the parameter ranges we consider (see Appendix A). We will thus make the simplifying assumption that $M_{\mathrm{H2}}(M) \propto M$ for the purposes of this section.

The HD(1-0) transition during the epoch of reionization falls into the frequency range of several upcoming intensity mapping experiments seeking to map reionization with the 158 μm [CII] transition, including FYST, the Tomographic Intensity Mapping Experiment (TIME, [46]), and the CarbON [CII] line in post-rEionization and ReionizaTiOn epoch project (CONCERTO, [47]). This coincidence means intensity maps of reionization-era HD will already exist in the data taken by these telescopes. Even in our most optimistic models, the HD line will be subdominant to the target [CII] line in all of these surveys. However, we can extract the HD line by constructing cross correlations between different frequency channels in these maps. As described in Ref. [48], the HD and [CII] lines will trace the same large-scale structure at different observed frequencies, so by correlating different frequency bands we can isolate both lines at the same redshift. The observed cross-spectrum in this case takes the form

$$P_{\mathrm{HD}\times[\mathrm{CII}]}(k,z) = \bar{I}_{\mathrm{HD}}(z)\bar{I}_{[\mathrm{CII}]}(z)\bar{b}_{\mathrm{HD}}(z)\bar{b}_{[\mathrm{CII}]}(z)P_m(k,z) + P_{\mathrm{HD}\times[\mathrm{CII}]}^{\mathrm{shot}}(z), \quad (19)$$

where $\bar{I}_{[\mathrm{CII}]}$ and $\bar{b}_{[\mathrm{CII}]}$ are the mean intensity and bias of the [CII] line, computed analogously to those of HD. The shot power in a cross correlation between two intensity mapping lines is given by

$$P_{\mathrm{HD}\times[\mathrm{CII}]}^{\mathrm{shot}}(k,z) = \int_{M_{\min}}^{M_{\max}} dM \frac{dn}{dM}(z) L_{\mathrm{HD}}(M) L_{[\mathrm{CII}]}(M) \times \left[\frac{y_X(z) D_{\mathrm{A}}(z)^2}{4\pi D_{\mathrm{L}}(z)^2}\right]^2, \quad (20)$$

as derived in Ref. [49].

Any measurement of the power spectrum will be cut off on large scales by the finite volume of a survey and on small scales by the finite instrument resolution. We account for the volume effects with a window function given by

$$W_X^{\mathrm{vol}} = \left(1 - \exp\left[-\left(\frac{k}{k_\perp^{\min}}\right)^2 (1-\mu^2)\right]\right) \times \left(1 - \exp\left[-\left(\frac{k}{k_\parallel^{\min}}\right)^2 \mu^2\right]\right), \quad (21)$$

and the resolution effects by

$$W_X^{\mathrm{res}} = \exp\{-k^2[\sigma_\perp^2(1-\mu^2) + \sigma_\parallel^2\mu^2]\}, \quad (22)$$

where the exact relations for $k_\perp^{\min}$, $k_\parallel^{\min}$, $\sigma_\perp$, and $\sigma_\parallel$ are given in Ref. [50] and μ is the cosine of the angle between a given mode vector and the line of sight. The full window function is then

$$W_X = W_X^{\mathrm{vol}} W_X^{\mathrm{res}}. \quad (23)$$

The error on the cross-power spectrum between two intensity maps is

$$\sigma_\times(k) = \frac{1}{\sqrt{N_{\mathrm{modes}}(k)}}[P_{\mathrm{HD}\times[\mathrm{CII}]}^2(k) W_{\mathrm{HD}}(k) W_{[\mathrm{CII}]}(k) + (P_{\mathrm{HD}}(k) W_{\mathrm{HD}}(k) + P_{\mathrm{HD}}^N)(P_{[\mathrm{CII}]}(k) W_{[\mathrm{CII}]}(k) + P_{[\mathrm{CII}]}^N)]^{1/2}, \quad (24)$$

TABLE I. Parameters for our reionization-era HD-[CII] cross-correlation forecasts at $z = 6$, including the overall sensitivity $\sigma_{\rm pix}$, the number of detectors $n_{\rm spec}$, the beam full width at half max $\theta_{\rm FWHM}$, the observing frequency $\nu_{\rm obs}$, the overall frequency bandwidth $\Delta\nu$, the channel width $\delta\nu$, the total observing time $t_{\rm obs}$, and the total survey area $\Omega_{\rm surv}$.

	FYST HD	FYST [CII]	FYST+ HD	FYST+ [CII]	Stage II HD	Stage II [CII]
$\sigma_{\rm pix}$ (MJy sr$^{-1/2}$ s$^{1/2}$)	2.1	0.50	2.1	0.50	0.044	0.089
$n_{\rm spec}$	20[a]	20[a]	200[a]	200[a]	16000	16000
$\theta_{\rm FWHM}$ (arcsec)	35	50	35	50	35	50
$\nu_{\rm obs}$ (GHz)	380	267	380	267	380	267
$\Delta\nu$ (GHz)	100	71	100	71	100	71
$\delta\nu$ (GHz)	3.8	2.7	3.8	2.7	2.5	2.5
$t_{\rm obs}$ (hr)	4000	4000	7000	7000	4000	4000
$\Omega_{\rm surv}$ (deg^2)	8.0	8.0	8.0	8.0	2.0	2.0

[a] FYST has ~6000 total detectors, but the effective number is reduced due to their use of a Fabry-Perot interferometer which cannot observe every frequency channel simultaneously [56]. We assume a similar configuration for FYST+.

where the $W_X(k)$ factors give the suppression of the signal at high k due to the finite instrument resolution and at low k due to the finite survey area [50], and

$$N_{\rm modes}(k) = \frac{k^2 \Delta k V_{\rm surv}}{4\pi^2} \tag{25}$$

is the number of independent Fourier modes available in a bin of width Δk for a survey covering total comoving volume $V_{\rm surv}$, accounting for the fact that only half of these modes are independent for a real field. The noise power spectrum of a map of X, denoted by P_X^N in Eq. (24), is given by Eqs. (B1)–(B3) in Appendix B.

The total signal-to-noise ratio (SNR) obtained over all k will then be

$$\mathrm{SNR} = \left[\sum_k \frac{P^2_{\mathrm{HD}\times[\mathrm{CII}]}(k) W_{\mathrm{HD}}(k) W_{[\mathrm{CII}]}(k)}{\sigma^2_\times(k)}\right]^{1/2}. \tag{26}$$

Note that Eqs. (24) and (26) only hold in the approximation of Gaussian statistics in both intensity maps at the scales of interest; this will not be true in the shot-noise regime, but the beam suppression factors $W_X(k)$ imply that the information obtainable from this regime is subdominant from that at larger scales.

Of the currently planned or in-progress [CII] experiments described above, FYST has the largest total frequency coverage, and thus offers the widest overlap between the [CII] and HD lines, so we will use it to represent the constraining power of current experiments. To demonstrate possibilities for future observations, we will also forecast for two examples of more advanced instruments. First, we consider a modest extension to FYST, such as may be attainable for a second-generation version of the experiment. We assign this "FYST+" survey an order of magnitude more detectors and a somewhat longer 7000 hour observing time. Second, to illustrate the scale of instrument which can confidently detect even our pessimistic model, we examine a light modification of the futuristic "Stage II" [CII] survey presented in Ref. [51]. This survey assumes an instrument with 16000 spectrometers. In terms of raw detector count, this is not an inconceivable increase over FYST, which has a ~6000-detector focal plane. However, FYST relies on a Fabry-Perot interferometer for spectroscopy which cannot observe its entire frequency range simultaneously. This gives FYST a performance per spectral channel equivalent to an instrument with only ~20 detectors. The "Stage II" concept would thus require a qualitative change in detector technology used for these surveys, perhaps derived from on-chip spectrometers currently under development [52–54].

The parameters we assume for these three surveys can be found in Table I. In the FYST frequency range, we get the best overlap between the two lines for a cross-correlation centered at $z = 6$. For FYST, we use the most up to date projections for their deep spectroscopic survey.[3] For the [CII] Stage II survey, we adjust the target frequency range as well as the frequency and angular resolutions to match FYST for ease of comparison. For both surveys, we model [CII] emission using model "m1" from Ref. [51], though it should be noted that the strength of the [CII] signal will likely be similarly uncertain.

Figure 2 shows the power spectra obtained by our optimistic and pessimistic radiative transfer models, compared to the sensitivities of the two experiments. For the FYST survey, we obtain an all-k SNR of 0.3 for the brightest of the two models. This puts the signal out of reach of current-generation experiments, though given the immense uncertainty in the signal amplitude even an upper limit may be interesting. The FYST + survey reaches

---

[3] Dongwoo Chung, private communication, see also Ref. [55].

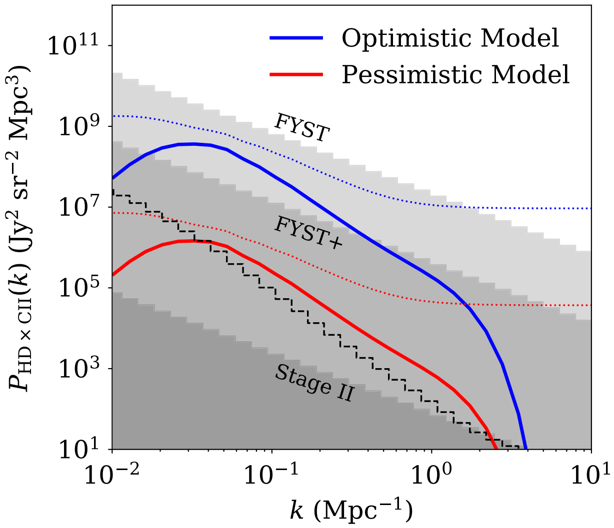

FIG. 2. [CII]-HD cross-power spectra at $z = 6$ assuming [CII] model “m1” from Ref. [51] and the optimistic (blue) and pessimisic (red) HD models described above. Dotted lines show the full, unsmoothed power spectra, solid lines show the spectra smoothed by the instrument resolution $W(k)$. Shaded regions show the sensitivity limits of the FYST (light shading), FYST+ (medium shading), and [CII] Stage II (dark shading) surveys defined in Table I. Noise levels assume Fourier bins of width $\Delta \log k = 0.1$, and the noise curves are plotted as “staircases” to show the widths of these bins. The gray bands show only the instrumental contribution to the power spectrum error, with no sample variance term included. For the sake of comparison, the black dotted line shows the total (noise + sample variance) error on the pessimistic model assuming the [CII]-Stage II setup.

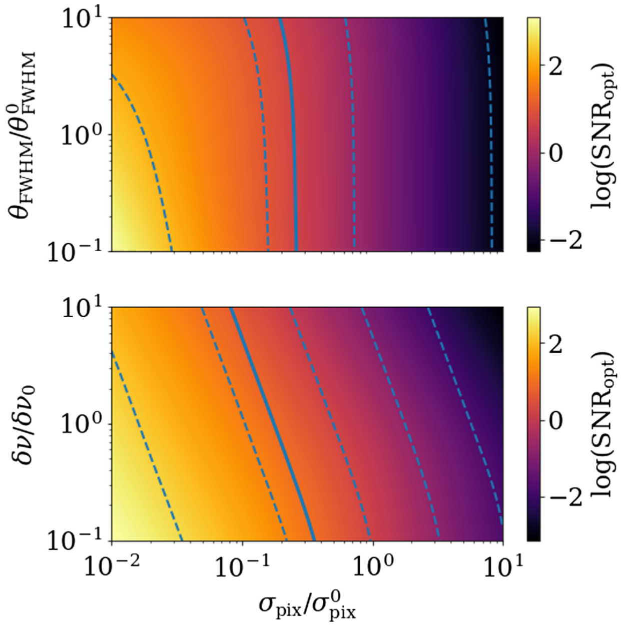

FIG. 3. Dependence of HD/[CII] cross-spectrum SNR on survey depth and resolution, both in the plane of the sky (top panel) and along the line of sight (bottom panel). We assume the noise level, beam FWHM, and frequency resolution are varied in the same way for both lines, though for an arbitrary experiment they could of course be varied independently. Central values σ^0_{pix}, θ^0_{FWHM}, and $\delta\nu_0$ are taken from the baseline FYST design from Table I, and SNR values assume the “optimistic” HD emission model. The blue solid lines denote the SNR = 5 contour, thinner dashed lines indicate the SNR = 0.01, 0.1, 1, 10, and 100 contours.

SNR ≈ 5 for the optimistic model, putting the brightest HD signals into range of reasonable expansions of current experiments. For the futuristic Stage II experiment, we find that even the fainter of the two models is detectable with a SNR of ∼11, making HD an excellent unique tracer of molecular gas during cosmic reionization. Our forecasts do not include systematics such as foreground subtraction, but we expect these systematics to affect [CII] and HD similarly, so that more detailed treatments for [CII] elsewhere in the literature should apply equally well to a [CII]-HD cross correlation.

Expanding beyond these specific experimental setups, Fig. 3 shows how the SNR for the FYST survey changes as we vary the angular and spectral resolution of the instrument as well as the instrument sensitivity σ_{pix}. We see that the detection significance is relatively insensitive to changes in the survey resolution, particularly in the plane of the sky. An order of magnitude improvement in spectral resolution is roughly equivalent to a factor of two improvement in σ_{pix}.

We will finally perform a rough requirements exercise to aid in the design of instruments aiming to detect the HD-[CII] cross correlation. If our primary goal is detection alone, we can neglect sample variance effects, simplifying Eq. (26) to

$$\mathrm{SNR} \approx \left[\sum_k N_{\mathrm{modes}}(k)\frac{P^2_{\mathrm{HD}\times[\mathrm{CII}]}(k)W_{\mathrm{HD}}(k)W_{[\mathrm{CII}]}(k)}{P^N_{\mathrm{HD}}P^N_{[\mathrm{CII}]}}\right]^{1/2}. \tag{27}$$

The shape of the power spectrum convolved with the two window functions is difficult to approximate further, but we have reduced the signal model here to an overall factor of $\bar{I}(z)$, and we argued in Fig. 3 that the resolution effects are subdominant to the noise and signal amplitudes. We can thus account for the most important factors by further simplifying to

$$\mathrm{SNR} \approx 5\left(\frac{\bar{I}_{\mathrm{HD}}}{100\,\mathrm{Jy/sr}}\right)\left(\frac{n_{\mathrm{spec}}}{200}\right)\left(\frac{t_{\mathrm{obs}}}{7000\,\mathrm{hr}}\right) \times\left(\frac{\sigma^{\mathrm{HD}}_{\mathrm{pix}}}{2.1\,\mathrm{MJy\,sr^{-1/2}\,s^{1/2}}}\right)\left(\frac{\sigma^{[\mathrm{CII}]}_{\mathrm{pix}}}{0.5\,\mathrm{MJy\,sr^{-1/2}\,s^{1/2}}}\right). \tag{28}$$

Equation (28) is only exactly valid for a survey with FYST’s volume and resolution. Note for comparison that $\bar{I}_{\mathrm{HD}}$ is roughly 250 times smaller for the pessimistic model than the optimistic value plotted here, so the sensitivity requirements would scale accordingly.

III. COSMIC DAWN

A. Gas cooling by hydrogen deuteride

An intensity mapping signal in HD(1-0) may also be generated by the halos that act as sites for formation of Population III stars. To see how this might arise, we first review the basic scenario for how these stars form (see Refs. [57,58] for reviews).

The first stars are typically expected to form at $z \sim 20$–30 in dark matter halos with $M \sim 10^6\ M_\odot$, based on the criteria that (1) the gravitationally bound gas is able to cool efficiently enough to collapse down to a protostellar core, and (2) the cosmic density field has a sufficient number of peaks that can collapse into halos of the appropriate mass. The virial temperature of the gas in such halos, $T_{\rm vir} \sim 2 \times 10^3 [(1+z)/20]$ K, is well below the threshold, $\sim 10^4$ K, at which substantial cooling can take place via atomic transitions. However, the residual free electrons left over from recombination are sufficient to catalyze the formation of H_2 with an abundance of $10^{-4} - 10^{-3}$, enough to allow the gas to cool down to roughly 200 K at $n \sim 10^4\ \mathrm{cm}^{-3}$. Once this limit (set by the lowest allowed rotational transition in H_2, 510 K) is reached, the rotational and vibrational levels in H_2 attain their LTE populations, and the H_2 cooling rate scales only linearly with number density (as opposed to the n^2 scaling at higher temperatures). From this point, cooling proceeds fairly slowly until the density reaches $10^8\ \mathrm{cm}^{-3}$, when three-body reactions begin to convert the rest of the H into H_2, and the interplay between different heating and cooling processes causes the gas to collapse further.

This picture changes somewhat when the role of HD is considered. The main chemical reaction that produces HD in the gas is exothermic, whereas the inverse reaction is endothermic; this leads to fractionation, which boosts the HD-to-H_2 ratio above the primordial D-H ratio, with a stronger boost at lower temperatures. If H_2 cools the gas to a sufficiently low temperature, enough HD can be produced that it will become the dominant coolant. Due to the smaller energy required to excite its first rotational state (128 K), HD can then allow the gas to cool almost down to the CMB temperature, until its critical density of $10^6\ \mathrm{cm}^{-3}$ is reached.

Several factors determine whether this will happen in a given halo. Simulations have shown that if the initial ionization fraction of the gas is no larger than that of the intergalactic medium (IGM) ($x_0 \sim 2 \times 10^{-4}$), halos with $M \gtrsim 10^6\ M_\odot$ will not form enough HD to significantly affect the gas cooling process [42,59–64], while HD-dominated cooling is seen in halos with the same ionization fraction but lower mass [42] or in halos that initially contain more ionized gas [42,61,65–69]. (The stars formed in these cases are often referred to as Population III.1, when the gas is of primordial composition, and Population III.2, when the gas has been partially ionized or otherwise affected by previous generations of objects.)

There are several possible mechanisms for increased ionization in these halos, including shocking by mergers or supernovae [61,66,68,70,71], proximity to relic HII regions [61,65,72], or the influence of far-ultraviolet background radiation or cosmic rays [68,69,73]. On the other hand, a UV background may instead act to dissociate HD and/or H_2, preventing molecular cooling from occurring within halos in a certain mass range [68,69,74–76], and the outcome can also depend on the detailed chemical processes that are included in a simulation [77]. Upcoming observations with the James Webb Space Telescope and Square Kilometer Array will be helpful in testing these different scenarios, but in the meantime, there will significant uncertainty in modeling the populations and properties of halos that might undergo HD cooling. In the following, we will consider two options—one more optimistic and one more pessimistic—for modeling the halo HD luminosity function, and take the difference between the two results as a rough indication of the modeling uncertainty.[4]

B. Modeling

To model the mean HD(1-0) intensity and power spectrum, we follow the approach of Ref. [38], which computes predictions for the same quantities arising from line emission from H_2 in the halos hosting Pop III stars. This approach also makes use of Eqs. (14)–(16) and (11) for computing the power spectrum, but with a different model for halo luminosities than we used for reionization in the previous section.

The halo mass-luminosity relation is written as

$$L_X(M,z) = 4\pi \int_0^{r_{\rm vir}(M,z)} dr r^2 n_X(r) \sum_Y n_Y(r) \Lambda(X,Y), \quad (29)$$

where $n_X(r)$ and $n_Y(r)$ are the number densities of X and Y at radius r within the halo and $\Lambda(X,Y)$ is the cooling coefficient for collisions of Y with X. The virial radius $r_{\rm vir}$ is given by Eq. (7) in Ref. [38].

When evaluating Eqs. (11) and (15)–(16), we follow Ref. [38] and set $M_{\rm min} = 10\ \mathrm{M}_\odot$. We also set $M_{\rm max} = 10^{13}\ \mathrm{M}_\odot$ for HD(1-0), and use the halo mass function from Ref. [79]. We use $r_{\rm min} = 1$ kpc as the lower integration bound in Eq. (29). The mean intensity and power spectrum integrals are computed with the public `lim` code.[5]

The HD level populations are dominantly affected by collisions with H, He, and H_2. Thus, it remains to model the density profiles of each of these, along with the associated cooling coefficients.

---

[4] See Ref. [78] for an alternative approach to modeling HD and H_2 emission from halos at cosmic dawn.

[5] https://github.com/pcbreysse/lim.

1. Density profiles

The density profiles of each species are related to the total gas profiles, which are observed in several simulations of the first stars (e.g., Refs. [42,62,67,69]) to follow

$$\rho_{\rm gas}(r) = \rho_0 \left(\frac{r}{r_0}\right)^{-2.2} \tag{30}$$

with $r_0 = 1$ pc and ρ_0 obtained from

$$M_{\rm gas} = 4\pi \int_0^{r_{\rm vir}} dr r^2 \rho_{\rm gas}(r) \tag{31}$$

with $M_{\rm gas} = (\Omega_{\rm b}/\Omega_{\rm m})M$. ($\rho_{\rm gas}$ thus depends on M and z, but we omit this dependence for brevity.) We can approximate the total gas number density as the sum of the number density of hydrogen and helium nuclei,

$$n_{\rm gas}(r) \approx n_{\rm H,nuc}(r) + n_{\rm He,nuc}(r), \tag{32}$$

where

$$n_{\rm H,nuc}(r) = \frac{f_{\rm H}\rho_{\rm gas}(r)}{m_{\rm H}}, \tag{33}$$

$$n_{\rm He,nuc}(r) = \frac{(1-f_{\rm H})\rho_{\rm gas}(r)}{m_{\rm He}}, \tag{34}$$

$f_{\rm H} = 0.739$ is the hydrogen mass fraction, and $m_{\rm H}$, $m_{\rm He}$ are the respective masses. We will ignore helium chemistry and take the number density of He atoms to equal that of He nuclei, $n_{\rm He}(r) = n_{\rm He,nuc}(r)$, while we compute the number density of atomic hydrogen via

$$n_{\rm H}(r) = n_{\rm H,nuc}(r) - 2n_{\rm H_2}(r). \tag{35}$$

[The $n_{\rm HD}/n_{\rm H_2}$ fraction never exceeds 0.05 in our model, so we can safely ignore HD in Eq. (35).]

For the H_2 and HD profiles, we use the results of Ref. [42], which simulated the evolution of primordial gas clouds starting from cosmological initial conditions, using an adaptive mesh refinement code and including deuterium reactions in their chemical network. In addition to simulations of “initially unperturbed“ (Pop III.1) gas, without any external ionizing sources, they considered an “initially ionized” (Pop III.2) case in which the gas becomes ionized at $z = 20$; although less realistic than a full radiative transfer treatment of the ionization, Ref. [42] argues that this approximation is expected to retain many of the features of a more detailed treatment. In this paper, we use separate models based on the initially unperturbed or ionized simulations, assuming that all halos belong to either one or the other category; these two cases represent pessimistic and optimistic scenarios for the strength of the HD intensity mapping signal, with the true signal likely somewhere in between. In the unperturbed case, Ref. [42] found that halos with $M \lesssim 10^6\ M_\odot$ exhibit much stronger HD cooling than those with $M \gtrsim 10^6\ M_\odot$, and we maintain this distinction in our predictions.

In detail, we take the simulation results for the H_2 mass fraction $X_{\rm H2}(r)$ from the simulated halos in Ref. [42],[6] and translate them into $f_{\rm H2}$, the number fraction of H_2, as a function of r,

$$f_{\rm H2}(r) \equiv \frac{n_{\rm H2}(r)}{n_{\rm gas}(r)} = \frac{\rho_{\rm gas}(r)}{n_{\rm gas}(r)}\frac{X_{\rm H2}(r)}{2m_{\rm H}}, \tag{36}$$

using $n_{\rm gas}(r)$ and $\rho_{\rm gas}(r)$ corresponding to the halos for which $X_{\rm H2}$ was measured. Then, since $n_{\rm gas}(r)$ is a monotonic function, we are able to use Eq. (36) to determine $f_{\rm H2}$ as a function of $n_{\rm gas}$.[7] This allows us to compute $n_{\rm H2}(r)$ for arbitrary halo mass, by inserting the appropriate $n_{\rm gas}(r)$ into

$$n_{\rm H2}(r) = f_{\rm H2}(n_{\rm gas}[r]) \times n_{\rm gas}(r). \tag{37}$$

When necessary, we further split this into profiles of ortho-H_2 and para-H_2, assuming them to be present in a 3:1 ratio. We then multiply Eq. (37) by the measurements of $n_{\rm HD}/n_{\rm H2}$ (as a function of $n_{\rm gas}$) from Ref. [42] to obtain the HD profiles, again using the separate results for initially unperturbed and ionized halos.

The upper panels of Fig. 4 show the predicted number density profiles of total gas, H_2, and HD for each type of halo in our model (initially unperturbed gas with $M < 10^6\ M_\odot$ and $> 10^6\ M_\odot$, and initially ionized gas), while the lower panels show the chemical abundances with respect to the total gas number density. These curves reflect the increased production of H_2 and HD for lower-mass initially-unperturbed halos, due to the generally lower temperatures in these halos as compared to those of higher mass, and the much larger production of these species when the gas is initially ionized, catalyzed by the larger abundance of free electrons [42].

2. Cooling coefficients

Following Refs. [38,81], for an optically thin line, the cooling coefficient $\Lambda(X, Y)$ can be written as

---

[6] For the initially unperturbed case, we use the results for Halo1-HD and Halo4-HD from Ref. [42], taking their H_2 mass fractions $X_{\rm H2}(r)$, $n_{\rm HD}/n_{\rm H2}$ ratios as a function of $n_{\rm gas}$, and gas temperatures $T(n_{\rm gas})$ to be representative of halos with masses above and below $10^6\ M_\odot$ respectively. For the initially ionized case, we take averages of these quantities over the four simulated halos from Ref. [42], since there are only minor differences between them.

[7] This procedure only allows us to determine $f_{\rm H2}(n_{\rm gas})$ for $n_{\rm gas} < 10^{12}\ {\rm cm}^{-3}$ using the results of Ref. [42]. For higher gas densities, we use the directly reported $f_{\rm H2}(n_{\rm gas})$ values reported in Ref. [38], derived from the simulations in Refs. [62,80].

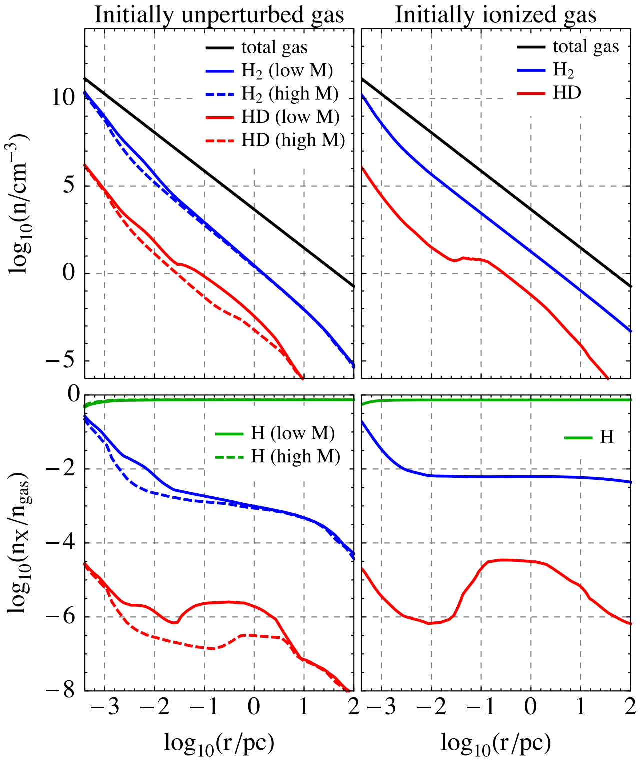

FIG. 4. Number density profiles (*upper panels*) and abundances (*lower panels*) for $M = 10^6\ M_\odot$ halos at $z = 15$, assuming formation from initially unperturbed gas (*left panels*) or initially ionized gas (*right panels*), based on the simulations of Ref. [42]. In the initially unperturbed case, we show different models corresponding to high-mass ($M \gtrsim 10^6\ M_\odot$) and low-mass ($M \lesssim 10^6\ M_\odot$) halos, the latter of which are seen to have higher H_2 and HD abundances in simulations. The initially unperturbed and ionized cases represent optimistic and pessimistic scenarios for modeling the HD intensity mapping signal from cosmic dawn.

$$\Lambda(X,Y) = \frac{\Lambda_{\rm LTE}(X,Y)}{1 + n_{\rm cr}(Y)/n_Y}, \tag{38}$$

where $\Lambda_{\rm LTE}(X,Y)$ is the cooling coefficient at local thermal equilibrium and $n_{\rm cr}(Y)$ is the critical density of Y required to reach LTE. The cooling coefficient at LTE is

$$\Lambda_{\rm LTE}(X,Y) = \frac{1}{n_Y} A_{JJ'} \frac{g_J}{g_{J'}} e^{-\frac{\Delta E_{JJ'}}{k_B T}} \Delta E_{JJ'}, \tag{39}$$

where $A_{JJ'}$ is the Einstein coefficient for the transition of interest, and our notation assumes that this transition is between two rotational levels J and J'. For HD(1-0), $A_{10} \approx 5.1 \times 10^{-8}\ {\rm s}^{-1}$ [40], $g_1 = 3$, $g_0 = 1$, and $\Delta E_{10}/k_B = 128$ K. We can approximate

$$\frac{n_{\rm cr}(Y)}{n_Y} \approx \frac{\Lambda_{\rm LTE}(X,Y)}{\Lambda_{n\to 0}(X,Y)}, \tag{40}$$

where the low-density cooling coefficient $\Lambda_{n\to 0}(X,Y)$ is

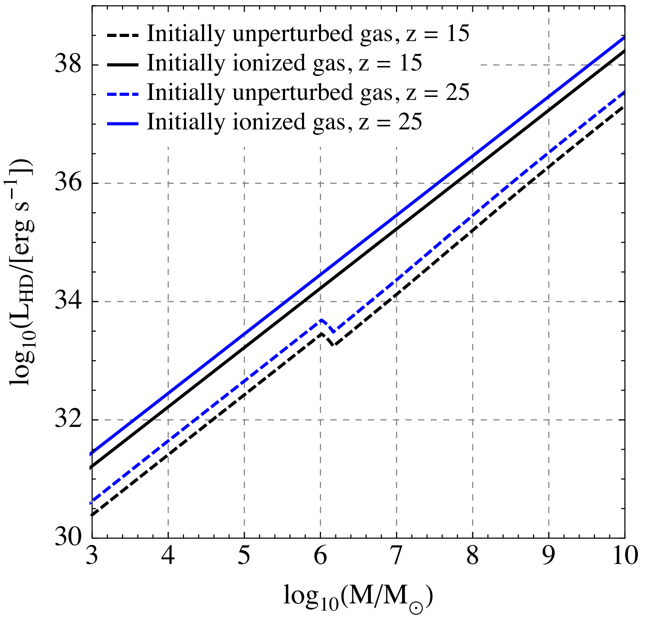

FIG. 5. Relationship between HD(1-0) luminosity and halo mass in our model for cosmic dawn, for initially unperturbed (*dashed*) and initially ionized (*solid*) gas clouds, and at two representative redshifts. This relationship is normalized higher in the initially unperturbed case for halos with $M \lesssim 10^6\ M_\odot$ than for higher masses, and is much higher for initially ionized halos, reflecting the increased HD abundance in those cases.

$$\Lambda_{n\to 0}(X,Y) = \kappa_{JJ'}(X,Y;T) \frac{g_J}{g_{J'}} e^{-\frac{\Delta E_{J\to J'}}{k_B T}} \Delta E_{J\to J'} \tag{41}$$

with $\kappa_{JJ'}(X,Y;T)$ the collisional deexcitation coefficient for $J \to J'$ in X in collisions with Y at temperature T. We obtain the gas temperature profiles $T(r)$ needed for Eqs. (39) and (41) by taking the $T(n_{\rm gas})$ measurements from the simulations in Ref. [42] and evaluating them on the $n_{\rm gas}(r)$ profiles for each halo mass we consider.

For HD colliding with H, He, and H_2, we use the collisional coefficients from Ref. [40],[8] which are based on fits to the original computations in Refs. [82,83]. For the 1-0 transition we are concerned with here, these rates are in excellent agreement with more recent computations [84–86].

Using the ingredients described above, the final $L_{\rm HD}(M,z)$ relations we compute in the initially unperturbed and ionized cases are shown in Fig. 5 at two different redshifts. As expected, we see much higher luminosities in the initially ionized case, due to the higher abundance of HD, as well as higher luminosities for initially unperturbed halos with $M \lesssim 10^6\ M_\odot$. The luminosities are higher at higher redshift, because a halo with a given mass is denser at earlier times (we use virial halo masses in our model, and the virial

---

[8] Available at http://ccp7.dur.ac.uk/cooling_by_HD/.

radius for a given mass is lower at earlier times). We show the analogous plot for $L_{\mathrm{H2}}(M,z)$ in Appendix B.

3. Consistency check

The radiative transfer model derived in Sec. II can only be computed out to redshift $z \lesssim 8$, as that is the limit of the simulations presented in Ref. [44]. We consider the models given in this section to be most accurate at $z \gtrsim 10$, because the ionizing background at lower redshifts will likely be strong enough to affect the HD abundances in the relevant halos in a way not captured by our models. However, we can still extrapolate our initially ionized and unperturbed models to check consistency with the previous section, though we will not use this extrapolation to make forecasts. Figure 6 shows the results of this extrapolation. We can clearly see that, when extended to the reionization era, both the ionized and unperturbed models give mean intensities within the range of radiative transfer models considered above. Thus, though our models are highly uncertain, they do show an encouraging level of consistency.

C. Detectability of cosmic-dawn signal

The HD(1-0) line from cosmic dawn falls conveniently into a frequency range observed by a variety of existing and planned cosmological measurements. We will demonstrate here that, though the signal modeled above is too faint for currently-planned surveys, it may be detectable with future instruments.

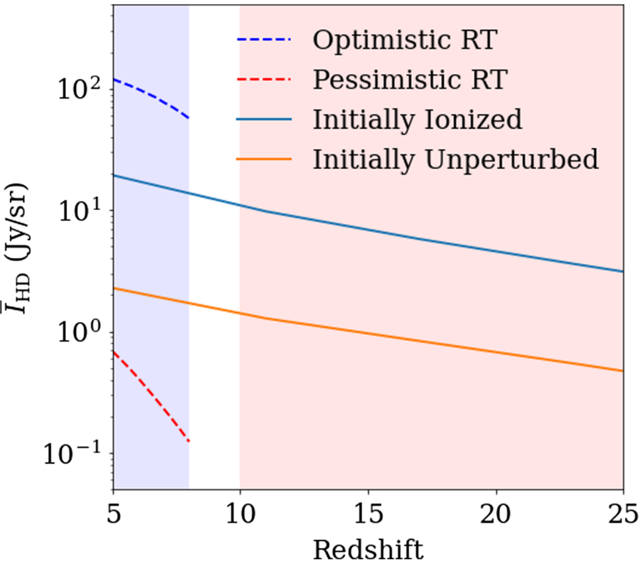

FIG. 6. Consistency check between the reionization-era models presented in Sec. II (dashed curves) and the cosmic dawn-era models presented in Sec. III (solid curves). The redshift ranges where we apply the models are shaded, with the cosmic dawn models extrapolated to lower redshifts for comparison. We note that the initially ionized (cyan) and initially unperturbed (orange) models lie in the range of the optimistic (blue) and pessimistic (red) radiative transfer models.

In this section, we forecast the (purely statistical) detection significance of the HD(1-0) power spectrum in the two models discussed above (initially unperturbed vs initially ionized). These two models serve as an extremely rough illustration of the uncertainty in the HD modeling at cosmic dawn, though of course the possibility remains for a significantly brighter or fainter signal. Under our current models, we find that current experiments cannot reasonably obtain signal-to-noise ratios better than $\mathcal{O}(10^{-2})$, putting detection out of reach for the near term. This is partially due to the essentially low amplitude of the signal, but also because existing instruments are poorly optimized for the HD observation.

Below we discuss the pros and cons of several existing and planned instruments for HD measurements, and discuss what it would take in each case for a detection. For details on the modeling of each experiment, see Appendix C. We remind the reader that we only consider statistical significance here, assuming that all systematics can be perfectly mitigated, so even seemingly hopeful SNR values will require further study to take various systematics into account.

1. ALMA

The cosmic-dawn era HD(1-0) line falls into ALMA bands 4 and 5, with the two bands spanning from redshift $z \sim 11$–20. ALMA has excellent overall sensitivity, and because it is an interferometer it has extremely high angular resolution, allowing for very deep surveys of small patches. ALMA has in fact already proven a capable tool for small-scale intensity mapping surveys [87], detecting the aggregate emission from several unresolved CO rotational transitions in band 3. The left panel of Fig. 7 shows ALMA sensitivities for a hypothetical HD survey centered at 142 GHz, or $z \sim 14$. Sensitivities assume a single 7.5 GHz frequency slice over a total survey area of 0.01 deg^2, chosen to optimize the trade-off between instrument noise and sample variance error.

However, ALMA has two key drawbacks which make it less suited to detecting cosmic-dawn HD. First, its high resolution is limited to very small survey areas. This means that it is primarily sensitive to smaller scales in the power spectrum (in other words, the large-scale cutoff in $W(k)$ from survey area appears at relatively high k). The HD power spectrum has very little shot noise at these redshifts (cf. the dotted unconvolved power spectra in Fig. 7), so the signal is quite low on these scales. Second, and more crucially, ALMA is not a dedicated survey instrument like the others we will consider in this section. For a 5σ detection of our brighter model, we would need to survey our field for ~9000 hours. This is not an unreasonable survey time for a dedicated CMB instrument, but it is completely unrealistic for an instrument as subscribed as ALMA.

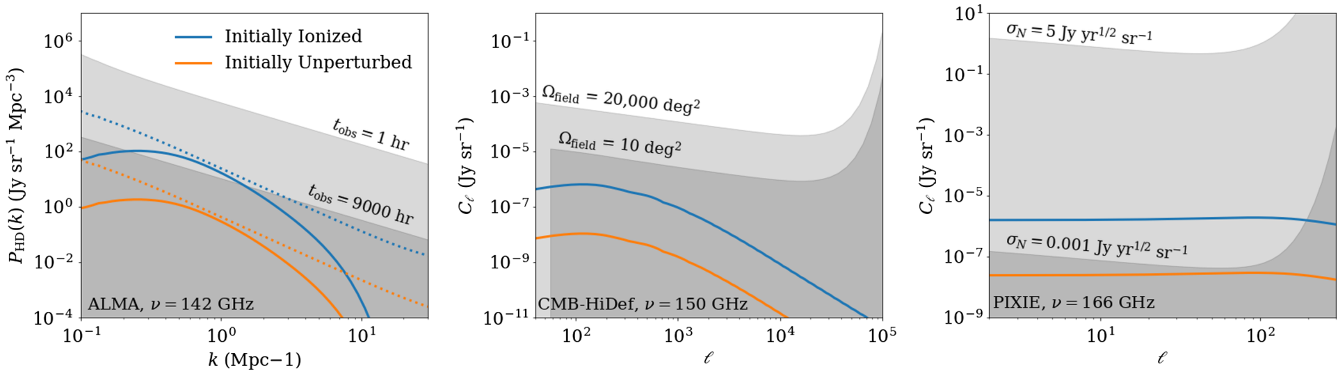

FIG. 7. Forecasted signals and sensitivities for cosmic-dawn era HD intensity mapping measurements. Power spectra (solid lines) are shown for the initially ionized (blue) and unperturbed (orange) models. *Left panel:* ALMA Band 4 observations over a 0.01 deg^2 field. Dotted lines show power spectra without instrumental resolution or finite-survey effects. The light gray band is the power spectrum error in bins of $\Delta \log k = 0.04$ for a single 1 hr pointing, the dark gray shows the same for a 9000 hr observation. The latter is necessary to obtain a 5σ detection of the ionized model. *Center panel:* CMB-HiDef observations, plotted as angular power spectra due to the large solid angle coverage. The light gray band shows the error for the planned ~half sky survey area, the dark band assumes the full observing time is spent on a 10 deg^2 field. The latter only obtains an overall SNR of ~1. *Right panel:* Space-based observations with a PIXIE-like instrument. The light gray band uses the planned PIXIE sensitivity, while the dark gray uses the substantially increased sensitivity from Ref. [37] to obtain a strong detection of both models.

2. Ground-based CMB instruments

Cosmic-dawn HD emission also falls into the frequency range of many CMB surveys. Unlike ALMA, these instruments are generally single-purpose survey projects, potentially allowing them to reach the depths required to detect the faint signal we model here. However, as a trade-off, these experiments do not have the same raw sensitivity of the ALMA interferometer.

The proposed CMB-High Definition (hereafter CMB-HiDef[9]) experiment [35] is likely to be the best of the near-future ground-based surveys for our purposes, due to its low noise levels (and because of its auspicious name). The proposed survey would cover roughly half of the sky for 7.5 years. Because the survey area is so large, the implicit flat-sky approximation we have used to compute 3D power spectra thus far is inadequate. In addition, CMB-HiDef (and most CMB surveys) do not have the spectral resolution of dedicated intensity mapping surveys, so the third dimension is largely unnecessary. We will instead forecast the 2D angular power spectrum C_ℓ for CMB-HiDef, which can be related to the 2D spectrum discussed thus far by

$$C_\ell = \frac{2}{\pi} \int dk k^2 P_{\rm HD}(k) \left[\int dr f(r) j_\ell(kr) \right]^2, \quad (42)$$

where j_ℓ is the spherical Bessel function and $f(r)$ is the radial window function of the survey.

For the CMB-HiDef frequency channel centered at 150 GHz, we obtain a signal-to-noise ratio of 0.02 integrated over all scales for the brighter of our two models. This is sadly still too low to be useful, and once again the primary issues stem from the fact that CMB-HiDef is not optimized for the HD measurement. Because the HD signal is so faint, a half-sky survey is much larger than ideal. If we assume the same survey time is spent on a 10 deg^2 field, the SNR rises to 0.75, which is still low, but a substantial improvement.

The other challenge comes from the lack of spectral resolution. The CMB is a 2D surface with smooth frequency evolution, so most experiments are designed around a few very wide frequency bands. The intensity mapping signal, however, is fully three dimensional, so many modes are lost with only wide frequency bands. On top of this, the primary means of removing foreground emission from an intensity map is to make use of the frequency structure of the signal. Though we do not directly model foregrounds here, this would provide another significant challenge for a broadband survey.

If we make the rough approximation that SNR scales with the square root of the number of frequency channels, then a version of CMB-HiDef with the bands split into $\mathcal{O}(50)$ channels could reach an SNR of 5 for the brighter model. Since increasing the frequency resolution is a much more substantial hardware change than simply varying survey area, we do not attempt a full forecast for this hypothetical modification of CMB-HiDef.

Finally, we note that CMB-HiDef has much better angular resolution than is actually required for the intensity mapping measurement. The intensity fluctuations we seek to measure trace the linear matter perturbations, which at these redshifts peak at $\ell \sim 100$. This point is similar to the argument from Fig. 3, which showed a weak dependence of SNR on angular resolution. Thus, if we were to do a

---

[9] We use CMB-HiDef as opposed to the more usual CMB-HD to avoid confusion with the HD molecule.

clean-sheet design of a CMB-HiDef-type experiment with spectral resolution, we would be free to trade off some of the angular resolution that gives CMB-HiDef its name.

3. CMB satellites

Orbiting CMB experiments have much more freedom in terms of frequency coverage than their ground-based equivalents due to the absence of atmospheric contamination. It is thus natural to examine whether any of these could detect HD as well.

Unfortunately, despite their advantages, most CMB satellites fall victim to the same difficulties as CMB-HiDef. Surveys optimized for CMB observations tend to cover large sky areas, creating very high noise levels for our faint HD signal. Also, again due to the broad-band nature of CMB emission, most surveys do not have particularly high frequency resolution. We performed forecasts for several current and proposed CMB satellites, including Planck [88], LiteBIRD [89], and PICO [90] (see Appendix C for the specifications we assume for each satellite). Of these surveys, the current best-estimate PICO setup gave the best SNR at cosmic dawn, rising to 0.002 for their 155 GHz channel for the initially ionized model. As with CMB-HiDef, this could potentially be improved by narrowing the survey area and adding frequency resolution, but not without dramatically altering the basic nature of the survey.

There is another proposed survey, however, which has a quite different design. The PIXIE survey [36] has a goal of measuring distortions to the blackbody shape of the CMB spectrum. Because of this, it has much finer frequency resolution than a typical survey, making it much better suited for intensity mapping measurements [91].

The combination of wide spatial coverage and high frequency resolution means that neither our $P(k)$ or C_ℓ formalisms are suited for forecasting PIXIE's sensitivity. A pure C_ℓ calculation on a single frequency channel would neglect all of the line of sight information, and a Cartesian $P(k)$ cannot be defined on a curved sky. We therefore approximate the sensitivity of PIXIE by computing the C_ℓ SNR per frequency channel, then scaling that by the square root of the number of channels to account for the line of sight information. This will not be as accurate as a full spherical 3D treatment [92], but the errors should be small compared to the large modeling uncertainty.

This extra resolution however comes at the cost of lower overall sensitivity. An all-sky PIXIE map spanning 15 GHz centered at 166 GHz obtains an extremely low SNR of $\sim 10^{-7}$, based on the sensitivities quoted in Ref. [36]. This could be improved somewhat by concentrating on a smaller survey area, but detection HD with the PIXIE design would likely require substantial improvements in overall sensitivity. For example, if we apply the extremely enhanced version of PIXIE designed in Ref. [37] to measure the time evolution of the CMB monopole, we obtain detections of both models. This statement assumes an identical survey to the baseline from Ref. [36], but with a 5000-fold increase in depth. Furthermore, this futuristic experiment would also likely have the statistical power to see the HD(1-0) *monopole*, since the range of our predictions for $\bar{I}_{\mathrm{HD}}$ from cosmic dawn [$\mathcal{O}(1)$ to $\mathcal{O}(10)$ $\mathrm{Jy\,sr^{-1}}$; see Fig. 6] are well above the monopole sensitivities computed for this experiment in Ref. [37] [$\mathcal{O}(10^{-3})$ to $\mathcal{O}(10^{-2})$ $\mathrm{Jy\,sr^{-1}}$; see their Fig. 2]. However, separation from other foregrounds would pose a significant challenge for such a measurement.

Finally, we note that the PIXIE frequency range covers the reionization-era HD discussed in the previous section as well. However, though our optimistic EoR model is somewhat brighter than our brightest cosmic-dawn model, it is not nearly bright enough to be detected with the baseline PIXIE configuration.

4. Cross correlations

Throughout the history of cosmology, one of the most effective ways to detect a faint signal has been to cross-correlate with an additional large-scale structure tracer. Cross correlations can improve signal-to-noise, and serve as an excellent tool for isolating a signal at a specific redshift from contaminating foregrounds. At the extreme redshifts considered here, there are not likely to be direct-imaging catalogs available for the foreseeable future, so the only likely target for cross correlations will be with other intensity mapping surveys. As cosmic dawn, by definition, occurs before significant star formation has taken place, there are very few emitting species to cross-correlate with. Two possible cross-correlation targets exist; the 21 cm hydrogen spin-flip transitions, and transitions from ordinary molecular hydrogen.

Across all redshifts, the 21 cm line is the most common target for intensity mapping. The HERA interferometer, currently operating in South Africa, has the ability to observe 21 cm photons from as far as redshift 20 [93], thus allowing for overlap with our hypothetical HD observations. In addition to helping detect HD, such a cross-correlation could provide significant science benefits to both surveys in the form of reduced foregrounds. Foregrounds are an immense challenge for 21 cm observations, often several orders of magnitude brighter than their signal [94]. For HD, a 21 cm correlation could make up for the lack of redshift resolution in a broadband CMB survey, similar to what was done in Refs. [95,96].

A 21 cm HD correlation would still likely require at minimum a more sensitive HD measurement than is currently possible, along the lines of the discussion in the previous section. HERA is targeting a first detection of high-redshift 21 cm, and is unlikely to obtain the kind of extremely high SNR that would be necessary to bring out the faint HD line.

Reference [38] proposed using intensity maps of H_2 transitions to map cosmic dawn. Though H_2 lacks the slight asymmetry that gives rise to rotational transitions in HD, its much greater abundance may lead to a signal bright enough to detect. Since the two lines will both come from early molecular clouds, an H_2 correlation would provide an excellent cross-check on an HD observation. The brightest H_2 line from cosmic dawn falls into the frequency range of the proposed Origins Survey Spectrometer [97]. Unfortunately, though Ref. [38] argued that a near-future experiment would have the potential to detect H_2, we find that an updated forecast with currently planned surveys does not have sufficient sensitivity (see Appendix B). Thus, while an HD-H_2 correlation is promising in principle, we would likely need mildly futuristic observations of both lines to reach cosmic dawn.

IV. DARK AGES

Finally, in this section we ask whether HD could be used for intensity mapping from the so-called dark ages ($z \gtrsim 30$), before the first stars formed. The most promising way to access this era of cosmic history is 21 cm intensity mapping [34,98,99], which will be rather difficult on its own, but given the amount of pristine cosmological information available during this epoch, it is worthwhile to explore other possible probes. Previously explored options for intensity mapping include hyperfine transitions in deuterium ($\lambda \approx 92$ cm), which could provide a measurement of the primordial [D/H] ratio if 92 cm maps are cross-correlated with 21 cm maps, although this will be difficult in practice [100]; or in $^3\mathrm{He}^+$ ($\lambda \approx 3.5$ cm), which will be essentially invisible during the dark ages due to the lack of contrast between the spin temperature in the IGM and the CMB temperature [101,102].

At $z \lesssim 60$, HD will be present in the IGM with $[\mathrm{HD/H}] \approx 4 \times 10^{-10}$ [32]; while this is tiny compared to the abundance of H, the spontaneous decay rate for HD(1-0) ($A_{10} \approx 5.1 \times 10^{-8}\ \mathrm{s}^{-1}$) is seven orders of magnitude higher than for the 21 cm transition ($A_{10} \approx 2.9 \times 10^{-15}\ \mathrm{s}^{-1}$). Furthermore, the signal would fall in the range between 40 and 90 GHz, which is already targeted by CMB experiments and will be much less impacted by the galactic synchrotron and ionospheric effects that will pose major obstacles for 21 cm measurements from the dark ages (although there will be other bright continuum foregrounds, most notably the CMB blackbody itself). With this in mind, we explore the HD case in more detail.

We wish to estimate the mean brightness temperature arising from HD(1-0) from the IGM, in contrast with the backlight CMB. This is given by (e.g., Ref. [103])

$$T_\mathrm{b}(z) = \frac{T_\mathrm{ex}(z) - T_\gamma(z)}{1+z}(1 - e^{-\tau}), \tag{43}$$

where T_γ and T_ex are the CMB temperature and the excitation temperature for the HD transition, respectively, and τ is the associated optical depth. This formula holds even outside of the Rayleigh-Jeans regime, as long as T_ex is very close to T_γ (which we will find to be the case here). The excitation temperature is defined by

$$\frac{n_1(z)}{n_0(z)} = \frac{g_1}{g_0} e^{-T_{10}/T_\mathrm{ex}(z)}, \tag{44}$$

where n_1 and n_0 are the number densities of the upper and lower states, and $T_{10} = 128$ K. The optical depth can be written as [100]

$$\tau = \frac{g_1}{g_1 + g_0} \frac{1}{8\pi} \frac{hc}{k_\mathrm{B} T_\mathrm{ex}(z)} \frac{A_{10}}{H(z)} \lambda_{10}^2 n_\mathrm{HD}(z), \tag{45}$$

where $H(z)$ is the Hubble parameter, assuming that the dominant source of line broadening is the Hubble flow.

Standard expressions for the excitation temperature of H cannot be directly applied to HD, because the Rayleigh-Jeans approximation for the blackbody intensity is not valid in this case. We must instead work forward from the equation for detailed balance of the upward and downward transitions [103],

$$n_1[C_{10} + A_{10} + B_{10} I_\gamma] = n_0[C_{01} + B_{01} I_\gamma], \tag{46}$$

where C_{10} is the collisional deexcitation rate of HD.[10] The Einstein B coefficients are related to A_{10} by

$$B_{10} = \frac{c^2}{2h\nu^3} A_{10}, \qquad B_{01} = \frac{g_1}{g_0} B_{10}, \tag{47}$$

while C_{01} and C_{10} are related by

$$\frac{C_{01}(z)}{C_{10}(z)} = \frac{g_1}{g_0} e^{-T_{10}/T_\mathrm{K}(z)}, \tag{48}$$

where T_K is the gas temperature, which we approximate as $T_\mathrm{K} \approx 0.02(1+z)^2$ K [32]. The rate C_{10} is a sum over particle species,

$$C_{10} = \sum_Y n_Y \kappa_{10}(\mathrm{HD}, Y; T), \tag{49}$$

where n_Y is the number density of species Y and κ_{10} is the same rate coefficient that appeared in Eq. (41). We consider collisions of HD with H and He in our numerical calculations, H_2 having a negligible effect. The radiation (CMB) intensity is a blackbody with temperature T_γ,

---

[10] For 21 cm at lower redshift, one must also account for the coupling between H and the UV radiation background (the so-called Wouthuysen-Field effect [104,105]). We are working at high enough redshift that we can ignore any possible analogous effect for HD.

$$I_\gamma(\nu, z) = \frac{2h\nu^3}{c^2} \frac{1}{\exp\left[h\nu/k_\mathrm{B}T_\gamma(z)\right] - 1}, \tag{50}$$

and we evaluate it and Eq. (47) at a frequency corresponding to T_{10}. We use $T_\gamma(z) = 2.725(1+z)$ K for the CMB temperature.

By combining Eqs. (44) and (46)–(50), we can solve for $T_\mathrm{ex}(z)$, and use the result in Eqs. (45) and (43) to obtain the mean brightness temperature. The result is that $T_\mathrm{b}(z)$ for HD(1-0) reaches a maximum of $\sim 10^{-15}$ K at $z = 60$. As points of reference, the 21 cm brightness temperature reaches a maximum (in absorption) of roughly 50 mK during the dark ages, with the corresponding number for the 92 cm D line being of order μK [100,103].

There are a few physical effects that act to suppress T_b down to such a small level. First, the excitation temperature remains tightly coupled to the CMB temperature in this epoch. For 21 cm, collisions drive the H excitation temperature towards the gas temperature at $30 \lesssim z \lesssim 150$. For HD, however, stimulated transitions by the CMB are much more efficient (due to the higher Einstein A value), while collisional excitation by the gas is much less efficient, due to the greater energy required ($\Delta E/k_\mathrm{B} = 128$ K, versus $\Delta E/k_\mathrm{B} = 0.068$ K for 21 cm). Numerically, this implies that T_ex does not differ from T_γ by more than 10^{-3} K at these redshifts. Second, despite the higher Einstein A value, the optical depth for these transitions is suppressed by the low HD abundance and shorter wavelength compared to 21 cm, resulting in a value of $\tau \approx 5 \times 10^{-11}$ at $z = 60$ (versus $\tau \approx 0.04$ for 21 cm).

Furthermore, when translating the $\mathcal{O}(10^{-15}\ \mathrm{K})$ brightness temperature to an intensity at a desired observing frequency (e.g., $\nu = 45$ GHz, or $T \approx 2.1$ K, for $z = 60$), one finds that the result is deep in the Wien tail of the blackbody distribution, implying an observed intensity that is suppressed by $\exp(-h\nu/k_\mathrm{B}T_\mathrm{b})$. This firmly places the signal beyond the reach of any conceivable experiment.

V. CONCLUSION

Reionization and cosmic dawn represent key unobserved frontiers in modern cosmology. We have discussed here a novel potential window into the high-redshift galaxies that drive reionization, the molecular clouds which birthed the earliest stars, and the intergalactic medium during the cosmic dark ages. While hydrogen intensity mapping is likely to remain the primary tracer of large-scale structure at extreme redshifts, HD could in principle represent a powerful complement to commonly discussed 21 cm intensity maps.

We have presented HD models covering reionization ($z \sim 6$–10), cosmic dawn ($z \sim 10$–30), and the dark ages ($z \gtrsim 30$). Of these regimes, we find (not unexpectedly) that the epoch of reionization represents the easiest target. While current [CII] intensity mapping experiments lack the sensitivity needed to detect HD, modest future improvements should bring the signal with reach through internal cross-correlations. Future designs should possess the statistical power to detect even our more pessimistic models (subject to appropriate control of systematics), adding HD to our ever-growing toolbox of reionization observations.

At cosmic dawn, where there are far fewer other observables available, we find that the HD signal is, while present, too weak to be detected by current experiments. There are many observatories designed for other purposes which cover the relevant frequencies, but none of them can detect even our most optimistic signal. Our forecast is less pessimistic for the near to moderate future however, with modest evolutions of current surveys able to begin cutting into the range of possible models.

Some hypothetical HD-sensitive instruments could include:

(i) An ALMA-like observatory capable of dedicating ~years of observing time to a deep intensity mapping survey,

(ii) A survey with CMB-HiDef-level sensitivity spent on a ~few deg^2 field, with modest spectral resolution, or

(iii) A futuristic, dramatically more sensitive spectroscopic CMB satellite, for example the enhanced version of the PIXIE satellite presented in Ref. [37].

The first two of these in particular are easily within the realm of present technology, though it may be some time before a dedicated HD measurement would justify the expense. The latter example requires more advancement, but would allow an HD measurement as part of a greater range of science goals. One could further improve the strength of an HD measurement by cross-correlating with either 21 cm or H_2 intensity maps, though future instruments would likely be necessary for these lines as well.

Finally, we studied the possibility of detecting a global IGM HD signal during the dark ages. As HD lacks the strong collisonal coupling that gives rise to a 21 cm dark ages signal, we find that there is no reasonably detectable signal from the precosmic-dawn era. The first molecular clouds at $z \sim 15$–30 thus represent the earliest detectable source of HD emission.

ACKNOWLEDGMENTS

We thank Matt Bradford, Yan Gong, Mat Madhavacheril, Margot Mandy, David Neufeld, Alexander van Engelen, and Dongwoo Chung for useful discussions. We acknowledge the support of the Natural Sciences and Engineering Research Council of Canada (NSERC). Research at Perimeter Institute is supported in part by the Government of Canada through the Department of Innovation, Science and Industry Canada and by the Province of Ontario through the Ministry of Colleges and Universities. J. M. is supported by the US Department of Energy under Grant No. DE-SC0010129. This research was undertaken, in part, thanks to funding from the Canada Research Chairs Program. L. C. K. acknowledges the support of a Beatrice and Vincent Tremaine Fellowship.

APPENDIX A: MASS-LUMINOSITY SCALING

When estimating power spectra for reionization-era HD from our radiative transfer models, we made the simplifying assumption that the HD luminosity of a halo scales linearly with its mass. We will show here that the potential error introduced due to this assumption is small compared to the other modeling uncertainties.

Our model gives an estimate for the sky-averaged mean intensity of the HD(1-0) line based on assumptions about the conditions within reionization-era molecular clouds (Eqs. (10)–(11)). We then need to decide how the HD emission is distributed among halos. To check the relative importance of this choice, we will compute power spectra for our "optimistic" and "pessimistic" models assuming five different halo mass scalings:

(a) The simple linear halo mass scaling used above.
(b) The same linear scaling, but with M_{min} dropped to $10^6\ M_\odot$ from $10^8\ M_\odot$.
(c) The scaling used for CO emission from Ref. [8], based on the star formation histories of Ref. [106].
(d) The same CO scaling, but with the 0.3 dex lognormal scatter between luminosity and halo mass used in Ref. [8] included.
(e) The scaling used for [CII] emission at reionization from Ref. [51]. We use their model "m2" as it is said to be the median of the four models presented.

While these scalings certainly do not capture the full range of possible behaviors, they do cover a wide range of possibilities. For each model, we enforce the overall mean normalization computing using Eqs. (10)–(11), then predict the updated bias and shot noise. The results are shown in Fig. 8 both with and without resolution effects included. We find that there can indeed be substantial differences between these models, particularly in the shot-noise regime. However, this difference does not outweigh the difference in mean intensities between the two models. On the scales we are sensitive to for FYST-like experiments, the effects of the mass scaling are entirely subdominant.

APPENDIX B: H_2 INTENSITY MAPPING AT COSMIC DAWN

In this appendix, we consider intensity mapping of H_2 at cosmic dawn using the 5-3 rotational transition, identified in Ref. [38] to be the most promising H_2 transition for detection.

We generally follow the modeling approach from Sec. III B, again taking the initially unperturbed and initially ionized cases as pessimistic and optimistic scenarios for the signal strength. We consider collisions of H_2 with H, He, and H_2, using the collisional coefficients from Ref. [107].[11] Figure 9 shows the resulting $L_{\mathrm{H2}}(M,z)$ for each case at $z = 15$ and 25. The H_2 halo luminosity relation is enhanced for higher-mass ($M \gtrsim 10^6\ M_\odot$) unperturbed halos, because of the higher temperatures and therefore higher cooling coefficients (see Eqs. (38)–(41) in these halos compared to lower-mass unperturbed halos, which is a stronger effect than the mildly increased H_2 abundances at lower masses (see Fig. 4). On the other hand, for the HD halo luminosities, the higher-HD abundance at lower halo mass is the dominant effect, resulting in an enhancement of L_{HD} at these lower masses (see Fig. 5).

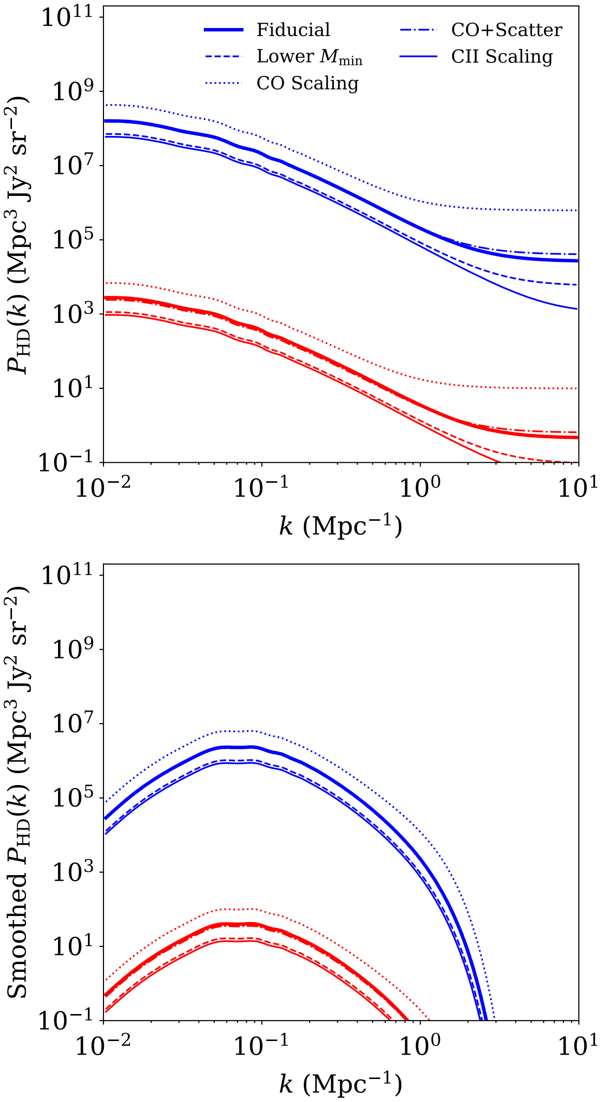

FIG. 8. Effect of the shape of the HD $L(M)$ relation on the power spectrum, both without (bottom) and with (top) instrumental effects included. The fiducial model linear model is plotted as the thick solid line, other possibilities include the same model with M_{min} reduced to $10^6\ M_\odot$ (dashed), the CO model from Ref. [8] with (dot-dashed) and without (dotted) scatter included, and the [CII] model from Ref. [51] (thin solid). Curves are plotted for the optimistic (blue) and pessimistic (red) radiative transfer models.

---

[11] Available at http://ccp7.dur.ac.uk/cooling_by_h2/.

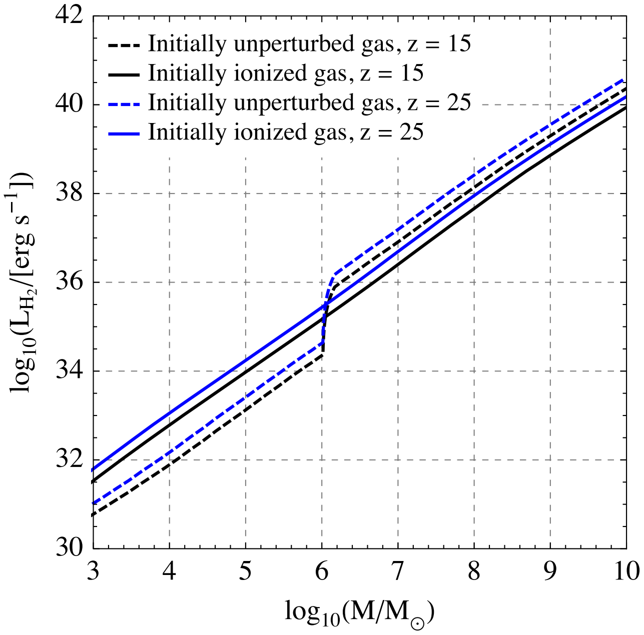

FIG. 9. Relationship between H_2 (5-3) luminosity and halo mass in our model for cosmic dawn, for initially unperturbed (*dashed*) and initially ionized (*solid*) gas clouds, and at two representative redshifts. In contrast to the HD results shown in Fig. 5, the relationship is enhanced for unperturbed halos with $M \gtrsim 10^6\ M_\odot$ compared to those of lower mass, because the higher temperatures in the more massive halos enhance the collisional cooling rate of H_2, and this dominates over the mild increase of H_2 abundance in lower-mass halos.

We consider an instrument designed to observe at the relevant wavelengths; the Origins Survey Spectrometer (OSS), which will cover 25 μm to 588 μm and is planned for the Origins Space Telescope [97]. We use OSS specifications from Table 3-1 in Ref. [97],[12] summarized in our Table II. We consider a 0.5 deg^2 survey lasting 1000 hours, based on the deep extragalactic survey planned for OSS.

We convert the above information into a 3D noise power spectrum $P_{\rm N}$ using [56]

$$P_{\rm N} = \frac{\sigma_{\rm pix}^2}{t_{\rm pix}} V_{\rm vox}, \tag{B1}$$

where $\sigma_{\rm pix}$ is the noise-equivalent intensity (NEI). The observing time per spatial pixel, $t_{\rm pix}$, is given by

$$t_{\rm pix} = \frac{n_{\rm pix} t_{\rm surv}}{\Omega_{\rm surv}/\Omega_{\rm pix}}, \tag{B2}$$

where $n_{\rm pix}$ is the number of spatial pixels, $t_{\rm surv}$ and $\Omega_{\rm surv}$ are the observing time and sky area for the entire survey, and $\Omega_{\rm pix}$ is the sky area per pixel. The comoving volume per observed voxel, $V_{\rm vox}$, is given by [109]

$$V_{\rm vox} = \chi(z)^2 y(z) \Omega_{\rm pix} \delta\nu, \tag{B3}$$

where $y(z) \equiv \lambda(1+z)^2 H(z)^{-1}$ converts from (rest) wavelength to radial distance and $\delta\nu$ is the frequency resolution.

Though Ref. [38] found that reasonably high-significance detections of the H_2 power spectrum might be possible with an instrument that is nominally similar to OSS, we find that the most up to date survey designs for OSS are not as sensitive as the example they used; specifically, we unfortunately find negligible SNRs for all of the observations we consider. For example, for an OSS map at 164 μm (corresponding to $z \sim 16$), we find a SNR of $\sim 2 \times 10^{-4}$ (see Fig. 10). Though this observation would overlap in redshift with the cosmic dawn HD measurements shown in Fig. 7, the fact that SNRs are low for both HD and H_2 means that even a cross-correlation between the two would not be able to isolate a signal. Thus, though H_2 remains one of the only other prereionization signals available, it would still require futuristic surveys to detect.

APPENDIX C: DETAILS OF COSMIC DAWN FORECASTS

In this appendix, we collect some details of how our forecasts for cosmic dawn were carried out.

TABLE II. Specifications of the Origins Survey Spectrometer (OSS) assumed in our forecasts for H_2 intensity mapping at cosmic dawn. We consider a 1000 hour survey of 0.5 deg^2.

Band	Band edges (μm)	Central redshift for H_2 (5-3)	NEI (MJy sr^{-1} s$^{1/2}$)	Beam FWHM (arcsec)	Number of spatial pixels	Spectral resolution (GHz)	$P_{\rm N}$ (Jy^2 sr^{-2} h^3 Mpc^3)
Band 3	[71, 124]	9.1	1.3	4.0	60	11	4.1×10^8
Band 4	[119, 208]	16	0.85	6.8	60	6.4	1.7×10^8
Band 5	[200, 350]	27	0.44	11	48	3.8	5.1×10^7

---

[12] Table 3-1 in Ref. [97] contains typos in the NEI values for bands 3 and 5, as well as a typo in the stated units [108]. Our values in Table II correspond to the corrected quantities.

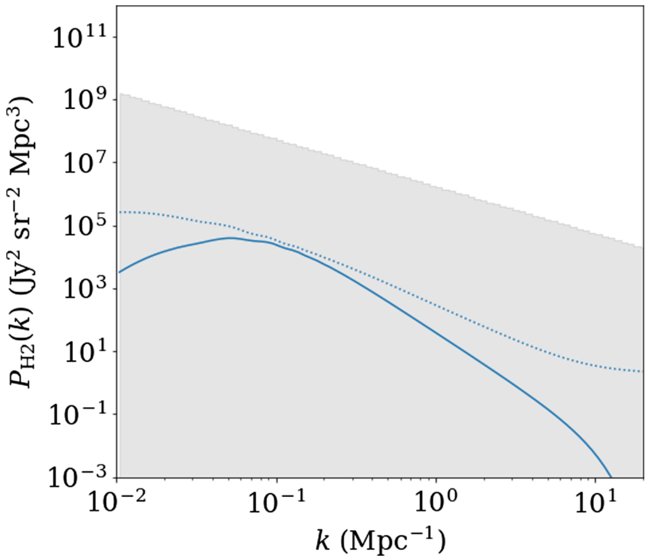

FIG. 10. H_2 power spectrum at $z \sim 16$ observed by OSS. Solid and dashed curves show the signal with and without instrument effects, the shaded region shows the OSS sensitivity. The all-scales SNR for this observation is $\sim 2 \times 10^{-4}$.

1. CMB experiments

For Planck, we used specifications from Table 4 of Ref. [88]. For PICO, we used the CBE specifications from Table 1.2 of Ref. [90], while for LiteBIRD, we used Table 1 of Ref. [89]; for both of these experiments, we divided the quoted map noise levels by $\sqrt{2}$ to convert from polarization to intensity. For PIXIE, we used the unpolarized sensitivity from Eq. (3.4) of Ref. [36], as well as the 15 GHz frequency resolution and equivalent 1.6° beam FWHM from their Table 1. For the "enhanced PIXIE" configuration, we assumed the same resolution and increased the sensitivity to the extremely high value from Ref. [37].

For CMB-HiDef, we used Table 1 of Ref. [110]. We assumed the 90 GHz and 150 GHz bands to have widths of 27 GHz (the same as the ACT 150 GHz band[13]), and the higher bands to have the same widths as those in FYST, taken from Fig. 2 of Ref. [111].

We summarize these specifications in Tables III and IV. Our noise power spectra for Planck, PICO, LiteBIRD, and CMB-HiDef can be obtained from the public `CMBnoise` code.[14]

TABLE III. Assumed specifications for the Planck and PICO CMB satellites in our forecasts for the HD signal from cosmic dawn. See Appendix C 1 for the corresponding references.

Instrument	Frequency (GHz)	Beam FWHM (arcmin)	Map noise level (μK arcmin)
Planck	28.4	32.3	150
	44.1	27.9	162
	70.4	13.1	210
	100	9.66	77.4
	143	7.22	33.0
	217	4.90	46.3
	353	4.92	154
	545	4.67	823
	857	4.22	3.03×10^4
PICO (CBE)	21	38	12.0
	25	32	9.19
	30	28	6.15
	36	24	3.96
	43	22	3.96
	52	18	2.83
	62	13	2.69
	75	11	2.12
	90	9.5	1.41
	108	7.9	1.13
	129	7.4	1.06
	155	6.2	0.919
	186	4.3	1.98
	223	3.6	2.26
	268	3.2	1.56
	321	2.6	2.12
	385	2.5	2.26
	462	2.1	4.53
	555	1.5	22.9
	666	1.3	88.9
	799	1.1	523

2. ALMA

In our forecasts for ALMA, we used configurations designed to match the characteristics of OSS, but mapped onto observations of HD instead of H_2, as closely as possible, to optimize for cross-correlations of the two tracers. For each frequency band of OSS, we mapped it onto the ALMA band(s) that could observe HD at the corresponding redshifts. For each such band, we then computed the sensitivity using the online ALMA sensitivity calculator,[15] with the following settings:

(a) *observing frequency*: central frequency of ALMA band.
(b) *bandwidth per polarization*: width of ALMA band divided by number of OST spectral pixels.
(c) *number of antennas*: 50 12 m antennas (we do not use the 7 m antennas because they result in a much larger noise power spectrum for intensity mapping).
(d) *resolution*: matched as closely as possible to OST beam FWHM values at equivalent frequency, within constraints of synthesized beams achievable by ALMA at given frequency.

---

[13] https://act.princeton.edu/technology/specifications.
[14] http://github.com/sjforeman/CMBnoise.
[15] https://almascience.nrao.edu/proposing/sensitivity-calculator.

TABLE IV. Assumed specifications for the LiteBIRD CMB satellite, along with the CMB-HiDef ground-based telescope, in our forecasts for the HD signal from cosmic dawn. See Appendix C 1 for the corresponding references.

Instrument	Frequency (GHz)	Beam FWHM (arcmin)	Map noise level (μK arcmin)
LiteBIRD	40	69	26.5
	50	56	17.0
	60	48	14.1
	68	43	11.5
	78	39	9.55
	89	35	8.27
	100	29	6.51
	119	25	5.37
	140	23	4.17
	166	21	4.60
	195	20	4.10
	235	19	5.44
	280	24	9.33
	337	20	13.8
	402	17	26.5
CMB-HiDef	30	1.25	6.5
	40	0.94	3.4
	90	0.42	0.7
	150	0.25	0.8
	220	0.17	2.0
	280	0.13	2.7
	350	0.11	100

TABLE V. ALMA configurations and sensitivities used in our forecasts for HD intensity mapping at cosmic dawn. We select configurations designed to match the angular resolution and number of frequency channels corresponding to each band of OSS considered in Table II, in order to optimize for H_2-HD cross-correlations. We use a fiducial time of 1 hour per single ALMA observation, and describe in the main text how to estimate the total observing time for a given intensity mapping survey.

ALMA band	Band edges (GHz)	Overlapping mid-IR band	Spectral resolution (GHz)	Synthesized beam width (arcsec)	Primary beam width (arcsec)	Sensitivity for 1 h observation (μJy beam^{-1})	P_N (Jy^2 sr^{-2} h^3 Mpc^3)
3	[84, 116]	OSS band 5	0.34	5.1	62	44	6.4×10^2
4	[125, 163]	OSS band 4	0.56	3.5	43	36	1.1×10^3
5	[158, 211]	OSS band 4	0.56	2.7	33	53	3.3×10^3
6	[211, 275]	OSS band 3	0.94	2.1	25	39	3.9×10^3
7	[275, 373]	OSS band 3	0.94	1.5	19	21	1.7×10^3

(e) *integration time*: 1 h (the resulting noise power spectrum can be scaled for other single-observation integration times by multiplying by $[1\ \mathrm{h}/t_{\mathrm{obs}}]$).

We convert the resulting sensitivity from μJy beam^{-1} to Jy sr^{-1} s$^{1/2}$ using the angular resolution and assumed (1 h) integration time per observation. We assume that a survey area greater than the field of view will be covered by mosaicked observations spaced by half the primary beam width. The information for each ALMA band, including the derived P_N, is summarized in Table V.

ALMA can observe a spectral window up to 7.5 GHz wide in a single observation. Thus, if time t_{obs} is devoted to a single observation, the total time to observe a sky area Ω over a spectral window of width $\Delta\nu$ is given by

$$t_{\mathrm{total}} = \left(\frac{\Omega}{[0.5\Delta\theta_{\mathrm{pr}}]^2}\right)\left(\frac{\Delta\nu}{7.5\ \mathrm{GHz}}\right)t_{\mathrm{obs}}, \tag{C1}$$

where $\Delta\theta_{\mathrm{pr}}$ is the primary beam width from Table V. The noise power spectrum corresponding to such a survey is the P_N value from Table V multiplied by $(1\ \mathrm{h}/t_{\mathrm{obs}})$.

[1] E. D. Kovetz *et al.*, arXiv:1709.09066.
[2] E. D. Kovetz *et al.*, Bull. Am. Astron. Soc. **51**, 101 (2020).
[3] E. Visbal, H. Trac, and A. Loeb, J. Cosmol. Astropart. Phys. 08 (2011) 010.
[4] J. R. Pritchard and A. Loeb, Rep. Prog. Phys. **75**, 086901 (2012).
[5] R. Ansari *et al.*, arXiv:1810.09572.
[6] R. C. Kennicutt, Jr. and N. J. Evans II, Annu. Rev. Astron. Astrophys. **50**, 531 (2012).
[7] A. D. Bolatto, M. Wolfire, and A. K. Leroy, Annu. Rev. Astron. Astrophys. **51**, 207 (2013).
[8] T. Y. Li, R. H. Wechsler, K. Devaraj, and S. E. Church, Astrophys. J. **817**, 169 (2016).
[9] P. C. Breysse, E. D. Kovetz, and M. Kamionkowski, Mon. Not. R. Astron. Soc. **457**, L127 (2016).
[10] G. C. Wick, Mem. Cl. Sei. Fis. Mat. Nat. **21**, 708 (1935).
[11] K. Pachucki and J. Komasa, Phys. Rev. A **78**, 052503 (2008).
[12] C. M. Wright, E. F. van Dishoeck, P. Cox, S. D. Sidher, and M. F. Kessler, Astrophys. J. Lett. **515**, L29 (1999).
[13] F. Bertoldi, R. Timmermann, D. Rosenthal, S. Drapatz, and C. M. Wright, Astron. Astrophys. **346**, 267 (1999).
[14] E. T. Polehampton, J.-P. Baluteau, C. Ceccarelli, B. M. Swinyard, and E. Caux, Astron. Astrophys. **388**, L44 (2002).
[15] S. K. R. Howat, R. Timmermann, T. R. Geballe, F. Bertoldi, and C. M. Mountain, Astrophys. J. **566**, 905 (2002).
[16] D. A. Neufeld, J. D. Green, D. J. Hollenbach, P. Sonnentrucker, G. J. Melnick, E. A. Bergin, R. L. Snell, W. J. Forrest, D. M. Watson, and M. J. Kaufman, Astrophys. J. Lett. **647**, L33 (2006).
[17] Y. Yuan, D. A. Neufeld, P. Sonnentrucker, G. J. Melnick, and D. M. Watson, Astrophys. J. **753**, 126 (2012).
[18] E. A. Bergin *et al.*, Nature (London) **493**, 644 (2013).
[19] A. V. Ivanchik, S. A. Balashev, D. A. Varshalovich, and V. V. Klimenko, Astron. Rep. **59**, 100 (2015).
[20] L. Spitzer, J. F. Drake, E. B. Jenkins, D. C. Morton, J. B. Rogerson, and D. G. York, Astrophys. J. Lett. **181**, L116 (1973).
[21] L. Spitzer, Jr., W. D. Cochran, and A. Hirshfeld, Astrophys. J. Suppl. Ser. **28**, 373 (1974).
[22] D. C. Morton, Astrophys. J. **197**, 85 (1975).
[23] S. Lacour, M. K. Andre, P. Sonnentrucker, F. Le Petit, D. E. Welty, J. M. Desert, R. Ferlet, E. Roueff, and D. G. York, Astron. Astrophys. **430**, 967 (2005).
[24] T. P. Snow, T. L. Ross, J. D. Destree, M. M. Drosback, A. G. Jensen, B. L. Rachford, P. Sonnentrucker, and R. Ferlet, Astrophys. J. **688**, 1124 (2008).
[25] C. Battersby *et al.*, Nat. Astron. **2**, 596 (2018).
[26] R. H. Cyburt, B. D. Fields, K. A. Olive, and T.-H. Yeh, Rev. Mod. Phys. **88**, 015004 (2016).
[27] R. I. Epstein, J. M. Lattimer, and D. N. Schramm, Nature (London) **263**, 198 (1976).
[28] T. Prodanovic and B. D. Fields, Astrophys. J. **597**, 48 (2003).
[29] R. J. Cooke, M. Pettini, and C. C. Steidel, Astrophys. J. **855**, 102 (2018).
[30] C. Pitrou, A. Coc, J.-P. Uzan, and E. Vangioni, Phys. Rep. **754**, 1 (2018).
[31] P. Ade *et al.* (Planck Collaboration), Astron. Astrophys. **594**, A13 (2016).
[32] D. Galli and F. Palla, Annu. Rev. Astron. Astrophys. **51**, 163 (2013).
[33] T. Herter *et al.*, Bull. Am. Astron. Soc. **51**, 213 (2019).
[34] A. Loeb and M. Zaldarriaga, Phys. Rev. Lett. **92**, 211301 (2004).
[35] N. Sehgal *et al.*, Am. Astron. Soc. **51**, 6 (2019).
[36] A. Kogut, D. J. Fixsen, D. T. Chuss, J. Dotson, E. Dwek, M. Halpern, G. F. Hinshaw, S. M. Meyer, S. H. Moseley, M. D. Seiffert, D. N. Spergel, and E. J. Wollack, J. Cosmol. Astropart. Phys. 07 (2011) 025.
[37] M. H. Abitbol, J. C. Hill, and J. Chluba, Astrophys. J. **893**, 18 (2020).
[38] Y. Gong, A. Cooray, and M. G. Santos, Astrophys. J. **768**, 130 (2013).
[39] L. Spitzer, *Physical Processes in the Interstellar Medium* (Wiley, New York, 1978).
[40] D. R. Flower, J. Le Bourlot, G. Pineau des Forêts, and E. Roueff, Mon. Not. R. Astron. Soc. **314**, 753 (2000).
[41] C. P. Endres, S. Schlemmer, P. Schilke, J. Stutzki, and H. S. P. Müller, J. Mol. Spectrosc. **327**, 95 (2016).
[42] I. D. McGreer and G. L. Bryan, Astrophys. J. **685**, 8 (2008).
[43] M.-A. Miville-Deschênes, N. Murray, and E. J. Lee, Astrophys. J. **834**, 57 (2017).
[44] C. D. P. Lagos, C. M. Baugh, C. G. Lacey, A. J. Benson, H.-S. Kim, and C. Power, Mon. Not. R. Astron. Soc. **418**, 1649 (2011).
[45] P. Ade *et al.* (Planck Collaboration), Astron. Astrophys. **571**, A30 (2014).
[46] A. T. Crites, J. J. Bock, C. M. Bradford, T. C. Chang, A. R. Cooray, L. Duband, Y. Gong, S. Hailey-Dunsheath, J. Hunacek, P. M. Koch, C. T. Li, R. C. O'Brient, T. Prouve, E. Shirokoff, M. B. Silva, Z. Staniszewski, B. Uzgil, and M. Zemcov, in *Millimeter, Submillimeter, and Far-Infrared Detectors and Instrumentation for Astronomy VII*, Society of Photo-Optical Instrumentation Engineers (SPIE) Conference Series Vol. 9153 (SPIE, Bellingham, WA, 2014), p. 91531W.
[47] G. Lagache, IAU Symp. **12**, 228 (2017).
[48] P. C. Breysse and M. Rahman, Mon. Not. R. Astron. Soc. **468**, 741 (2017).
[49] R. H. Liu and P. C. Breysse, Phys. Rev. D **103**, 063520 (2021).
[50] J. L. Bernal, P. C. Breysse, H. Gil-Marn, and E. D. Kovetz, Phys. Rev. D **100**, 123522 (2019).
[51] M. Silva, M. G. Santos, A. Cooray, and Y. Gong, Astrophys. J. **806**, 209 (2015).
[52] E. M. Barrentine, G. Cataldo, A. D. Brown, N. Ehsan, O. Noroozian, T. R. Stevenson, K. U-Yen, E. J. Wollack, and S. H. Moseley, in *Millimeter, Submillimeter, and Far-Infrared Detectors and Instrumentation for Astronomy VIII*, Society of Photo-Optical Instrumentation Engineers

(SPIE) Conference Series Vol. 9914, edited by W. S. Holland and J. Zmuidzinas (SPIE, Bellingham, WA, 2016), p. 99143O.
[53] A. Endo, K. Karatsu, A. P. Laguna, B. Mirzaei, R. Huiting, D. J. Thoen, V. Murugesan, S. J. C. Yates, J. Bueno, N. v. Marrewijk, S. Bosma, O. Yurduseven, N. Llombart, J. Suzuki, M. Naruse, P. J. de Visser, P. P. van der Werf, T. M. Klapwijk, and J. J. A. Baselmans, J. Astron. Telesc. Instrum. Syst. **5**, 035004 (2019).
[54] K. S. Karkare, P. S. Barry, C. M. Bradford, S. Chapman, S. Doyle, J. Glenn, S. Gordon, S. Hailey-Dunsheath, R. M. J. Janssen, A. Kovács, H. G. LeDuc, P. Mauskopf, R. McGeehan, J. Redford, E. Shirokoff, C. Tucker, J. Wheeler, and J. Zmuidzinas, J. Low Temp. Phys. **199**, 849 (2020).
[55] M. Aravena *et al.* (CCAT-Prime Collaboration), arXiv: 2107.10364.
[56] D. T. Chung, M. P. Viero, S. E. Church, and R. H. Wechsler, Astrophys. J. **892**, 51 (2020).
[57] S. C. O. Glover, The first stars, in *The First Galaxies*, Astrophysics and Space Science Library (Springer-Verlag, Berlin, Heidelberg, 2013), p. 103.
[58] V. Bromm, Rep. Prog. Phys. **76**, 112901 (2013).
[59] V. Bromm, P. S. Coppi, and R. B. Larson, Astrophys. J. **564**, 23 (2002).
[60] F. Nakamura and M. Umemura, Astrophys. J. **569**, 549 (2002).
[61] J. L. Johnson and V. Bromm, Mon. Not. R. Astron. Soc. **366**, 247 (2006).
[62] N. Yoshida, K. Omukai, L. Hernquist, and T. Abel, Astrophys. J. **652**, 6 (2006).
[63] E. Ripamonti, Mon. Not. R. Astron. Soc. **376**, 709 (2007).
[64] H. Kreckel, H. Bruhns, M. Čížek, S. C. O. Glover, K. A. Miller, X. Urbain, and D. W. Savin, Science **329**, 69 (2010).
[65] T. Nagakura and K. Omukai, Mon. Not. R. Astron. Soc. **364**, 1378 (2005).
[66] T. H. Greif, J. L. Johnson, R. S. Klessen, and V. Bromm, Mon. Not. R. Astron. Soc. **387**, 1021 (2008).
[67] S. Hirano, T. Hosokawa, N. Yoshida, H. Umeda, K. Omukai, G. Chiaki, and H. W. Yorke, Astrophys. J. **781**, 60 (2014).
[68] D. Nakauchi, K. Inayoshi, and K. Omukai, Mon. Not. R. Astron. Soc. **442**, 2667 (2014).
[69] S. Hirano, T. Hosokawa, N. Yoshida, K. Omukai, and H. W. Yorke, Mon. Not. R. Astron. Soc. **448**, 568 (2015).
[70] Y. A. Shchekinov and E. O. Vasiliev, Mon. Not. R. Astron. Soc. **368**, 454 (2006).
[71] J. Prieto, R. Jimenez, and L. Verde, Mon. Not. R. Astron. Soc. **437**, 2320 (2014).
[72] N. Yoshida, S. P. Oh, T. Kitayama, and L. Hernquist, Astrophys. J. **663**, 687 (2007).
[73] J. Jasche, B. Ciardi, and T. A. Ensslin, Mon. Not. R. Astron. Soc. **380**, 417 (2007).
[74] Z. Haiman, T. Abel, and M. J. Rees, Astrophys. J. **534**, 11 (2000).
[75] J. Wolcott-Green and Z. Haiman, Mon. Not. R. Astron. Soc. **412**, 2603 (2011).
[76] E. Visbal, Z. Haiman, B. Terrazas, G. L. Bryan, and R. Barkana, Mon. Not. R. Astron. Soc. **445**, 107 (2014).
[77] S. C. O. Glover and T. Abel, Mon. Not. R. Astron. Soc. **388**, 1627 (2008).
[78] B. Novosyadlyj, V. Shulga, Y. Kulinich, and W. Han, Astrophys. J. **888**, 27 (2020).
[79] J. L. Tinker, A. V. Kravtsov, A. Klypin, K. Abazajian, M. S. Warren, G. Yepes, S. Gottlober, and D. E. Holz, Astrophys. J. **688**, 709 (2008).
[80] K. Omukai, Astrophys. J. **546**, 635 (2001).
[81] D. Hollenbach and C. F. McKee, Astrophys. J. **855**, 102 (2018).
[82] D. R. Flower and E. Roueff, Mon. Not. R. Astron. Soc. **309**, 833 (1999).
[83] E. Roueff and C. J. Zeippen, Astron. Astrophys. **343**, 1005 (1999), https://ui.adsabs.harvard.edu/abs/1999A%26A...343.1005R/abstract.
[84] J. L. Nolte, P. C. Stancil, T.-G. Lee, N. Balakrishnan, and R. C. Forrey, Astrophys. J. **744**, 62 (2012).
[85] N. Balakrishnan, J. F. E. Croft, B. H. Yang, R. C. Forrey, and P. C. Stancil, Astrophys. J. **866**, 95 (2018).
[86] B. Desrousseaux, C. M. Coppola, M. V. Kazandjian, and F. Lique, J. Phys. Chem. A **122**, 8390 (2018).
[87] G. K. Keating, D. P. Marrone, G. C. Bower, and R. P. Keenan, Astrophys. J. **901**, 141 (2020).
[88] Y. Akrami *et al.* (Planck Collaboration), Astron. Astrophys. **641**, A1 (2020).
[89] M. Hazumi *et al.*, J. Low Temp. Phys. **194**, 443 (2019).
[90] S. Hanany *et al.* (NASA PICO Collaboration), arXiv: 1902.10541.
[91] E. R. Switzer, Astrophys. J. **838**, 82 (2017).
[92] A. Liu, Y. Zhang, and A. R. Parsons, Astrophys. J. **833**, 242 (2016).
[93] D. R. DeBoer *et al.*, Publ. Astron. Soc. Pac. **129**, 045001 (2017).
[94] A. Liu, M. Tegmark, J. Bowman, J. Hewitt, and M. Zaldarriaga, Mon. Not. R. Astron. Soc. **398**, 401 (2009).
[95] A. R. Pullen, P. Serra, T.-C. Chang, O. Doré, and S. Ho, Mon. Not. R. Astron. Soc. **478**, 1911 (2018).
[96] S. Yang, A. R. Pullen, and E. R. Switzer, Mon. Not. R. Astron. Soc. **489**, L53 (2019).
[97] M. Meixner *et al.*, arXiv:1912.06213.
[98] J. O. Burns *et al.*, arXiv:1902.06147.
[99] S. Furlanetto *et al.*, arXiv:1903.06212.
[100] K. Sigurdson and S. R. Furlanetto, Phys. Rev. Lett. **97**, 091301 (2006).
[101] J. S. Bagla and A. Loeb, arXiv:0905.1698.
[102] M. McQuinn and E. R. Switzer, Phys. Rev. D **80**, 063010 (2009).
[103] S. Furlanetto, S. P. Oh, and F. Briggs, Phys. Rep. **433**, 181 (2006).
[104] S. A. Wouthuysen, Astrophys. J. **57**, 31 (1952).
[105] G. B. Field, Proc. Inst. Radio Eng. **46**, 240 (1958).
[106] P. S. Behroozi, R. H. Wechsler, and C. Conroy, Astrophys. J. **770**, 57 (2013).
[107] J. Le Bourlot, G. Pineau des Forêts, and D. R. Flower, Mon. Not. R. Astron. Soc. **305**, 802 (1999).
[108] C. M. Bradford (private communication).
[109] Y. Gong, A. Cooray, M. Silva, M. G. Santos, J. Bock, M. Bradford, and M. Zemcov, Astrophys. J. **745**, 49 (2012).
[110] N. Sehgal *et al.*, arXiv:2002.12714.
[111] S. K. Choi *et al.*, J. Low Temp. Phys. **199**, 1089 (2020).